Università degli Studi di Padova
Dipartimento di Fisica ed Astronomia "Galileo Galilei"
Corso di Laurea Magistrale in Fisica


# First extraction and acceleration operations of negative ion beams produced in NIO1 experiment

Relatore: dott. Gianluigi Serianni
Correlatore: dott. Barbara Zaniol
Controrelatore: dott. Marco Mazzocco

Laureando: Marco Zanini
1104450

Anno Accademico 2015/2016

*Alla mia famiglia*
*A Margherita*

**Abstract**

The research and the development of a Neutral Beam Injector as an auxiliary heating system is fundamental for ITER, the experimental reactor under construction in Cadarache (France) as a worldwide collaboration. This thesis work was performed on NIO1 experiment, developed at Consorzio RFX in collaboration with INFN-LNL. It consists in a radiofrequency negative ion source, with a maximum extracted current of 130 mA in $H^-$ ions, accelerated up to 60 kV by a three-grids system and it constitutes the testbed for the source of ITER neutral beam injector.
In this work, the first NIO1 operation with beam extraction is described and analyzed, in order to provide a beam characterization, using expecially electrical measurements.
In *chapter 1* a brief introduction about fusion physics and ITER is presented, with more emphasis regarding the external heating systems, while in *chapter 2* an overview of NIO1 experiment is proposed. The following chapters review the effect of radiofrequency power and gas pressure on total extracted current. The analysis treats separatly the current of negative ions and of electrons, extracted from the beam source together with the ions. Operations with oxygen as a filling gas are reported in *chapter 3*, while hydrogen operations are described in *chapter 4*. At the end of this chapter a comparison between the two gasses will be performed.
In *chapter 5* two ways are used to estimate the electron density: the first is based on a spectroscopical analysis of oxygen-argon emission lines. An alternative method, based on the Langmuir probe physics was developed and a comparison with spectroscopy measurements was performed.
In *chapter 6* conclusions are reported.

**Sommario**

La ricerca e lo sviluppo di un iniettore di fasci neutri come sistema di riscaldamento è fondamentale per il progetto ITER, il reattore sperimentale in costruzione a Cadarache (Francia), frutto di una collaborazione mondiale. Il lavoro svolto durante questa tesi è basato sull'esperimento NIO1, sviluppato presso il Consorzio RFX in collaborazione con INFN-LNL. L'esperimento consiste in una sorgente a radiofrequenze di ioni negativi, con una corrente massima estraibile pari a 130 mA ad un'energia di 60 keV, la quale costituisce il banco di prova per la sorgente dell'iniettore di ITER.
Nel *Capitolo 1* verrà presentata una breve introduzione sulla fisica della fusione e sul progetto ITER, mentre nel *capitolo 2* verrà presentato l'esperimento NIO1. I capitoli seguenti analizzano gli effetti prodotti da potenza fornita e pressione della sorgente sugli ioni. L'analisi tratta separatamente la corrente di ioni negativi ed elettroni, estratti dalla sorgente assieme agli ioni. Le operazioni in ossigeno sono riportate nel *capitolo 3* mentre quelle in idrogeno sono descritte nel *capitolo 4*. Alla fine di questo capitolo verrà effettuato un confronto tra i due gas.
*capitolo 5* verranno esposti due metodi usati per stimare la densità elettronica: il primo è basato su una analisi spettroscopica delle linee di emissione di una miscela di Ossigeno-Argon. Un metodo alternativo, basato sulla fisica della sonda di langmuir è stato sviluppato e confrontato con i risultati della spettroscopia.
Nel *capitolo 5* verranno riportate le conclusioni.

# Contents


**1 Introduction** **1**
- 1.1 Nuclear fusion and ITER project . . . 1
- 1.2 Plasma heating systems . . . 8
- 1.3 Neutral Beam Injector . . . 8
  - 1.3.1 Source Plasma Heating . . . 10
  - 1.3.2 Negative Ion Production . . . 11
  - 1.3.3 Acceleration . . . 13

**2 NIO1 experiment** **17**
- 2.1 Description of the experimental apparatus . . . 18
- 2.2 Diagnostic systems . . . 22
- 2.3 Database and Raspberry calibration . . . 25

**3 Oxygen operations** **27**
- 3.1 Reflected Power . . . 29
- 3.2 Electron Current . . . 29
  - 3.2.1 RF input power and source pressure . . . 30
  - 3.2.2 Filter and Bias . . . 34
- 3.3 Ion Current . . . 36
  - 3.3.1 RF input power and Source Pressure . . . 37
  - 3.3.2 Acceleration voltage . . . 43
  - 3.3.3 Filter and Bias . . . 45
- 3.4 IR thermocamera . . . 47

**4 Hydrogen operations** **49**
- 4.1 Reflected Power . . . 50
- 4.2 Electron Current . . . 51
- 4.3 Ion Current . . . 54
  - 4.3.1 Comparison between H and O ion current . . . 58
- 4.4 Bias System . . . 61
- 4.5 IR thermocamera . . . 62

**5 Electronic density estimations** **63**
5.1 Spectroscopy . . . . . 63
5.2 Electrical data . . . . . 66

**6 Conclusions** **71**

**Appendices** **75**

**A Bias Plate and Filter configuration** **77**

**B Reflected Power and density estimation** **81**

# Chapter 1

# Introduction

## 1.1 Nuclear fusion and ITER project

The increasing global energy demand requires the developement of alternative sources, in order to produce energy without an excessive impact on the environment. In fact, fossil fuel energy production is no longer sustainable because of the excessive pollution and the continous decrease of global reserves while renewable sources can not sustain alone the energy demand. Nuclear fission energy production yields a low carbon dioxide production, but fissile fuel storage decreases and nuclear wastes have to be stored for thousands of years.
A solution can be represented by nuclear fusion: two light nuclei can be bound together to create an heavier nucleus and the difference of binding energy is equal to the produced energy. The Coulomb repulsion between nuclei is very strong and particles need to reach high energy to get close enough so that the Strong Interaction overcomes the electrostatic force: a little probability to overcome the potential barrier exists due to the Tunnel Effect; in particular, the statistical fluctations of the Maxwell-Boltzmann distribution and quantum mechanical effects allow the fusion of the nuclei, even if the average kinetic energy is lower than the potential barrier.
Several exothermic fusion reactions are known; the present fusion research is focused on the deuterium-tritium (D-T) reaction due to the higher cross section with respect to other reactions: in figure 1.1b, the reactivity, defined as $\langle \sigma v \rangle$, is reported as a function of temperature. Total energy is divided between helium and neutron kinetic energy, as reported in the following equation:

$$D + T =^4 He(3.5MeV) + n(14.1MeV) \tag{1.1}$$

While deuterium is available in water, tritium is an unstable isotope with a short lifetime (about 12 years). However, it can be produced from Lithium, which is widespread on the earth crust. This element easily reacts with the incoming neutrons

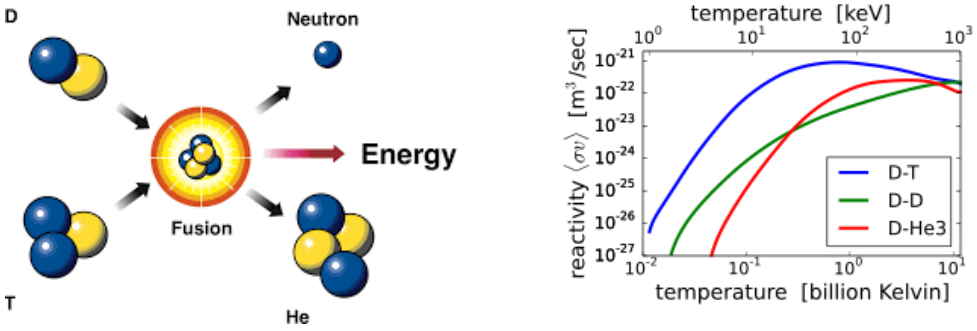


(a) Scheme of D-T reaction

(b) Reactivity for different fusion processes

Figure 1.1

and the main reactions are:

$$^{6}Li + n \rightarrow T +^{4} He + 4.8 \text{ Mev} \tag{1.2}$$

and

$$^{7}Li + n \rightarrow T +^{4} He + n - 2.5 \text{ MeV} \tag{1.3}$$

Nowadays, fusion research in mainly focused on two lines of research:

- Inertial Confinement: A target composed of deuterium and tritium is compressed by high power LASERs that allow nuclei to overcome the Coulomb barrier. An example is given by the National Ignition Facility, which operates in the USA
- Magnetic Confinement: Charged ionized particles are confined by high magnetic fields. This topic will be presented in this introduction.

Several ways were conceived for the magnetic confinement: in 1950's, the Tokamak configuration was developed in USSR and due to the high reached performances it is considered the most promising configuration to achieve nuclear fusion.
Tokamaks are toroidal machines in which plasmas are confined by a strong toroidal magnetic field and a lower poloidal field to avoid drifts that can lead to a separation of species, with the raising of an electric field between them, that can create an **E** $\times$ **B** drift, which can lead to the loss of plasma. [4]
The first component is produced by several toroidal coils; while the second is induced by an axial coil: this coil generates a magnetic flux change, that induces an electromotive force which creates a toroidal current. This current generates the poloidal magnetic field and also contributes to plasma heating due to Joule dissipation.
In a toroidal configuration, produced helium nuclei are supposed to cede energy to deuterium or tritium nuclei through collisions, while neutrons, that can not be magnetically confined due to their neutral charge, will cede their energy to the blanket:

in this way, kinetic energy is transformed into thermal energy.
For an ion and electron plasma at temperature $T$, the energy per unit volume is $w = 3nT$ and it can be expressed as the following equation:

$$\frac{\mathrm{d}w}{\mathrm{d}t} = p_H + p_\alpha - p_L - p_R \tag{1.4}$$

where $p_H$ is the external injected power to heat plasma, $p_\alpha$ represents the contribution given by produced $\alpha$-particles, $p_R$ is the power loss by electromagnetic radiation and $p_L$ is the power loss trough other processes (generally, convection and conducuction). The power (per unit volume) delivered to the plasma by $\alpha$ particles produced by fusion reactions (with deuterium and tritium divided into equal portions), can be written as:

$$p_\alpha = \frac{1}{4} n^2 \langle \sigma v \rangle E_\alpha \tag{1.5}$$

where $n$ is the plasma density, $\langle \sigma v \rangle$ is the reactivity (reported in Figure 1.1b and $E_\alpha = 3.5$ MeV is the energy of the $\alpha$-particles produced by fusion reactions.

The power loss by electromagnetic radiation can be divided between *bremsstrahlung* emission and line emission. The last contribution can be neglected if a D-T plasma is considered; however a large contribution can be provided by impurities.
*Bremsstrahlung* power loss (per unit volume) can be written as:

$$p_b = \alpha_b n^2 T^{1/2} \ \mathrm{Wm}^{-3} \tag{1.6}$$

where the constant $\alpha_b = 5.35 \times 10^{-37}$ W m$^3$ keV$^{-1/2}$.

The most difficult contribution to be quantified is the power loss by transport processes; it can be parametrized by the introduction of a parameter named confinement time:

$$P_L = \frac{W}{\tau_E} \tag{1.7}$$

where W is the total thermical plasma energy. In steady conditions, if fusion reactions can be neglected, an external energy $\mathrm{P}_H = \mathrm{P}_L + \mathrm{P}_R$ has to be delivered to the plasma. In those conditions, by equation 1.4, $\tau_E$ can be experimentally written as:

$$\tau_E = \frac{W}{P_H - P_R} \tag{1.8}$$

The former equation provides a first way to extrapolate the confinement time, however no fusion reaction nor total energy variation were considered.
Several scale laws were developed; for istance, for ohmic Tokamak, the neo-Alcator law [4]:

$$\tau_E(\mathrm{s}) = 0.07 a R_0^2 q_a \kappa^{0.5} n \tag{1.9}$$

where $R_0$ and $a$ are the major and minor radius, $q_a$ is the safety factor at the edge and $\kappa$ is the elongation factor.

If the power delivered by produced $\alpha$-particles is enough to compensate for total power losses, the *ignition* condition is obtained: in this condition, there is no need to use external power sources and the plasma is self-substained; using former written relation, the ignition is reached if:

$$n\tau_E > \frac{12T}{\langle\sigma v\rangle E_\alpha - 4\alpha_b T^{1/2}} \tag{1.10}$$

Considering that radiation losses are reduced in these temperature ranges and that in the same ranges $\langle\sigma v\rangle \propto T^2$, the ignition condition becomes:

$$nT\tau_E > 3 \times 10^2 \mathrm{m}^{-3}\mathrm{keVs} \tag{1.11}$$

However, if more realistic density and temperature profile are considered, the latter can be written as:

$$nT\tau_E > 5 \times 10^2 \mathrm{m}^{-3}\mathrm{keVs} \tag{1.12}$$

An useful factor is Q defined as the ratio between the produced fusion power and the injected power:

$$Q = \frac{P_f}{P_H} \tag{1.13}$$

The condition in which $\mathrm{Q} = 1$ , named *break-even* happens when the energy produced in fusion reaction in equal to the inserted power. If the ignition is reached, $\mathrm{P}_H = 0$ , $\mathrm{Q} \to \infty$. Not all the produced fusion power can be converted in energy: in fact, as formerly discussed, part of the energy is ceded to $\alpha$ particles, which contributes to plasma heating.

The ignition is the most convenient regime for a thermonuclear reactor; however a net gain of energy can be obtained also with the help of external heating systems.

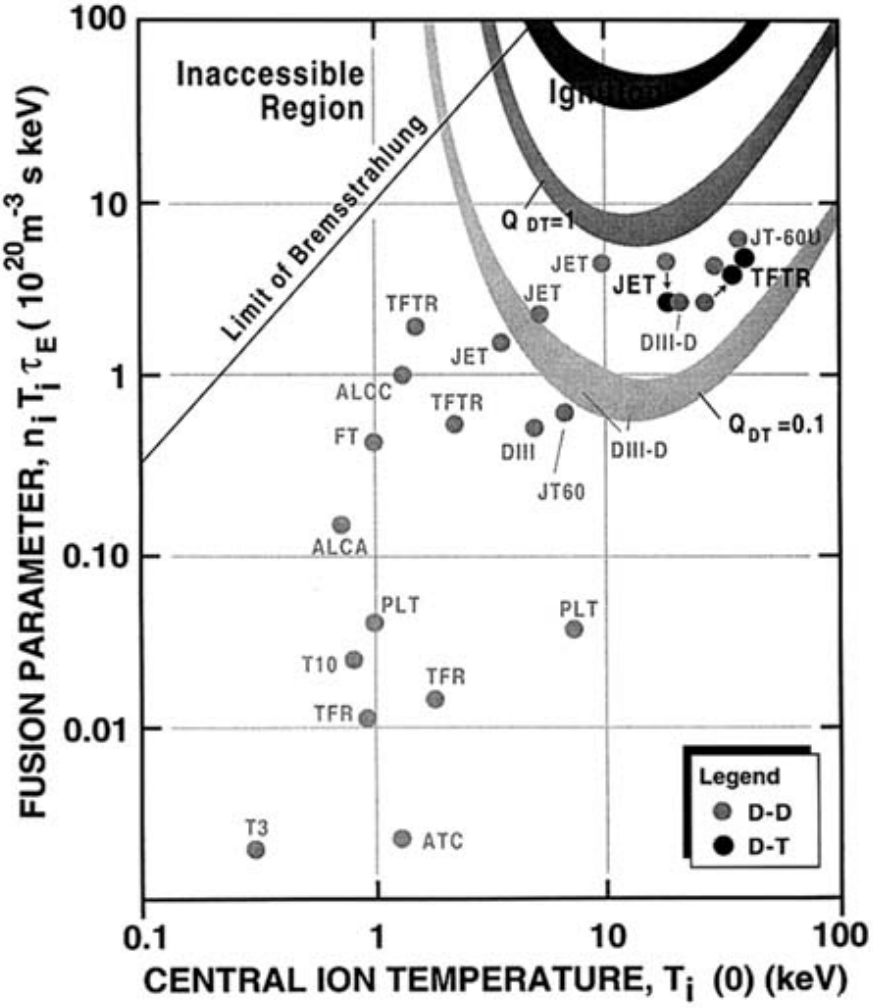


Figure 1.2: The value of the triple product for which ignition can be reached is represented by the black curve. Moreover, the best results of the more important fusion experiments are reported.

The ITER project (figure 1.3) was estabilished in order to demostrante the feasibility of fusion reactions for civilian purposes.

The first project aim is to obtain an energy gain factor Q, such that $5 < Q < 10$ in stationary conditions. The magnetic field is mainly produced by superconductive coils placed around the vessel, but a contribution is provided by the driven current in the plasma. It is expected to produce a fusion power of 500 W, with a pulse duration up to 500 s and a Q value at least of 10.

In ITER a gas composed of deuterium and tritium will be used and the energy pro-

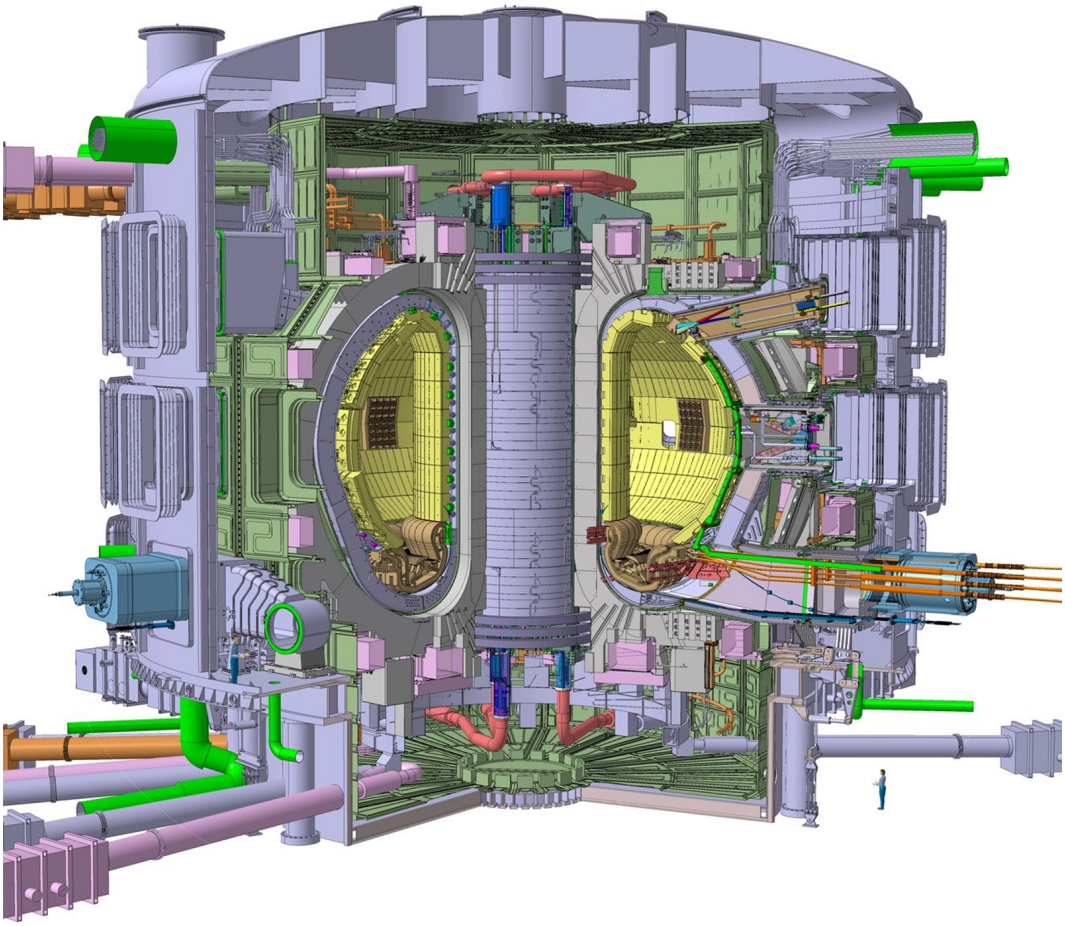

Figure 1.3: ITER

duced in the reaction (eq. 1.1) is divided between Helium (3.6 MeV) and neutrons (14.1 MeV); the latter are not affected by the magnetic fields, since they have no electric charge, therefore they can not be confined. The produced neutron flow will impact on the blanket, converting their kinetic energy into thermal energy; in a reactor this energy can be turned into electrical energy. This component requires suitable materials: the first wall is planned to be constituted of Beryllium, to reduce the losses due to impurity line radiation. The rest has to be composed of high-strenght copper and stainless steel, to make the blanket resistant to mechanical stresses and to shield the vessel and the superconductive coils from the neutron flux. [1]
Once the feasibility of fusion as a civilian energy will be demonstrated, a further generation of experimental reactors, such as DEMO, will be realised and neutrons

energy will be converted in electrical energy.
In first phases, tritium will be externally inserted; however, in the later experimental phase, prototype breeding modules will be used to test materials for "*Tritium Breeding*", because it is not possible to externally satisfy the tritium requirements, therefore it is necessary that the TOKAMAK produces it, using the produced neutrons.

| ITER parameters | | |
|---|---|---|
| Major Radius | 6.2 | [m] |
| Minor Radius | 2 | [m] |
| Fusion Power | 500 | [MW] |
| External Power | 50 | [MW] |
| Q | $\geq 10$ | |
| ITER Height | 26 | [m] |
| ITER radius | 29 | [m] |
| Maximum Toroidal field in axis | 5.3 | [T] |
| Plasma Current | 5.3 | [MA] |
| Pulse Lenght | $\geq 400$ | [s] |
| Plasma Volume | 837 | [$m^3$] |

Table 1.1: Main ITER parameters

## 1.2 Plasma heating systems

To reach the threshold temperture that allows fusion reactions to happen, the plasma has to be heated and there are several methods to increase the temperature. Since the plasma can be considered as a conductor material, high intensity currents are generated by the magnetic field used to confine it, thus causing ohmic heating. However, its resistivity depends on temperature as $T^{-3/2}$. Therefore, as the temperature increases, the resistance (and the heating effects) drops. For these reasons external heating systems are required for ITER in order to provide 50 MW of heating power. A way to insert external power is provided by the injection of microwaves, generated outside the TOKAMAK and coupled, through suitable antennas, to the plasma to whom they cede energy. Keeping in mind that cyclotronic frequency of a charged particles is:

$$\omega = \frac{eB}{m} \tag{1.14}$$

and considering that the toroidal magnetic field decreases as $1/R$, where $R$ is the minor radius, it is possible to heat a localized area by changing the input wave frequency. Three main processes will be used [4]:

- **ICRH** ($30 - 100$ MHz): Waves propagated from the lower magnetic field zone to higher field zone. A fast magnetosonic wave is generated and it propagates until the resonance area is reached, where wave energy is delivered to ions.
- **LH** ($1 - 8$ GHZ): A *lower hybrid* wave is generated by *klystron*. At these frequencies, the most importand process is constituted by *Landau Damping*. It is a non-collisional process that creates a current by accelerating electrons: in this way it is possible to generate and to substain the toroidal current.
- **ECRH** ($100 - 200$ GHz): *Gyrotrons* are used to generate millimetric waves, which propagates until the zone in which the electron cyclotron resonance condition is verified, where the energy is ceded to electrons.

The second method consists of the injection of energetic particles, in order to heat the plasma through collisions. Consorzio RFX was called to develop the prototype of injectors that will be used in ITER: for this purpose, PRIMA [14] (**P**adova **R**esearch **I**TER **M**egavolt **A**ccelerator) facility has been estabilished. It will host two experiment: SPIDER (**S**ource for the **P**roduction of **I**on of **D**euterium **E**xtracted from an **R**F plasma) which is the prototype of the ion source that will be used for the complete injector, MITICA (**M**egavolt **I**TER **I**nejctor **A**nd **C**oncept **A**dvance). The neutral beam injector wil be discussed in the next section.

## 1.3 Neutral Beam Injector

The injection of high-energy particles provides to heat the plasma through collisions. Particles need to be neutral, since charged particles should be deflected by the

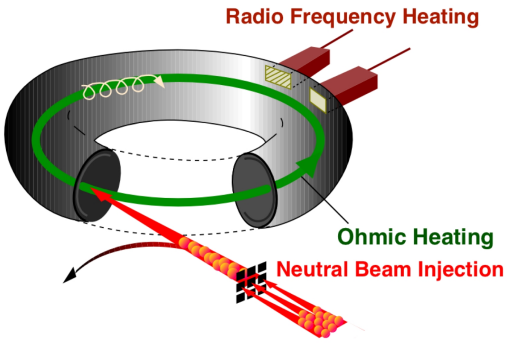


Figure 1.4: Example of heating systems in a TOKAMAK

TOKAMAK magnetic field and would not reach the plasma. Schematically, ions are produced in the source and they are extracted and accelerated through a grid system. The beam, neutralized through collisions, is finally injected in the TOKAMAK and ionized by plasma particles. Since the beam particle temperature is higher than that of the plasma particles, they cede energy through collisions.
Negative ions are produced inside the ion source. Produced ions are then extracted from the source through an acceleration system, composed by several grids biased at different electrical potential. ITER shall require 16.5 MW of power, so a 40 A $D^-$ ions current needs to be extracted; to achieve this extracted current, it is expected to obtain a current density of 280 A/$m^2$, accelerated up to an energy of 1 MeV. Since after 100 keV the neutralization cross section becomes too low, as can be seen in figure 1.5, it is necessary to employ other methods. For this reasons, negative ion beams are preferred, since negative ions have higher neutralization cross section with respect to positive ones and they can ensure about a 60 % of neutralized particles. The ITER injector prototype, named MITICA, is under construction.

| MITICA parameters | | |
|---|---|---|
| Beam Energy | 1 | [MeV] |
| $D^-$ Current | 40 | [A] |
| Current Density | 280 | [$Am^{-2}$] |
| Ion Extraction Area | 0.2 | [$m^2$] |
| Operating Pressure | $< 0.30$ | [Pa] |
| Electron/Ions | $\simeq 1$ | |

Table 1.2: MITICA parameters [11]

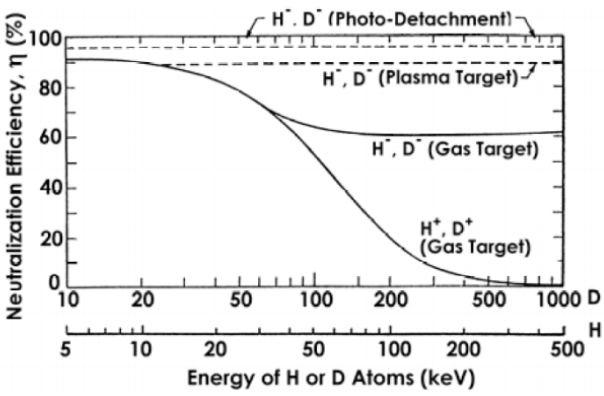


Figure 1.5: Neutralization cross section as a function of the energy, for different hydrogen ions.

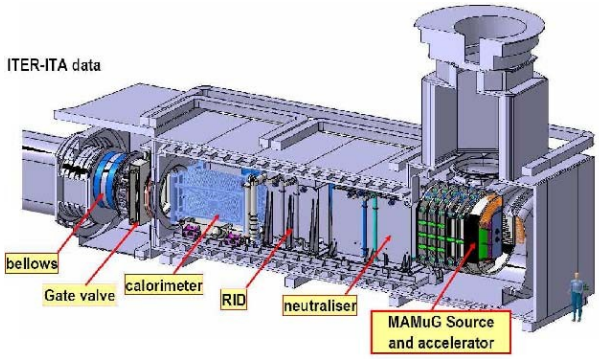


Figure 1.6: MITICA device

### 1.3.1 Source Plasma Heating

High power beams are needed for ITER plasma heating: such high power ion beams require that the plasma generator efficiently generates a dense and uniform plasma over a wide area. Two configuration have been developed:

- In the first configuration, the source is composed of hot cathode, usually a tungsten filament which emits electrons due to the thermoionic effects. The plasma is generated by collisions between the background gas and the emitted electrons, which are accelerated towards the anode. The main problem of this source type is that the cathode has a short lifetime and it needs periodically replacements.

- In the second one, the plasma is inductively coupled by applying a coil wound around the source fed by a generator.

MITICA source will be based on the second process. In its source the plasma is produced by a radiofrequency generator, using an inductively coupled plasma (ICP) and it is confined by a multipolar cusp magnetic field. In ICP, source power is ceded from the RF electric field to the plasma through two different processes: a collisional ohmic dissipation and a collisionless stochastic heating [13].
The first process is caused by collisions between electrons and neutral particles or ions: its collision frequency can be divided into three components:

$$\nu_c = \nu_{en}^{(p)} + \nu_{en}^{(ion)} + \langle \nu_{ei}^{(p)} \rangle \tag{1.15}$$

First two terms are related to electron - neutral collision, corresponding, respectively, to the collision frequencies for the momentum- transfer ($\nu_{en}^{(p)}$) and for electron-neutral ionization ($\nu_{en}^{(ion)}$).
The third collision frequency is related to the momentum loss for electron-ion collisions. Neglecting the ion motion, it can be expressed as:

$$\langle \nu_{ei}^{(p)} \rangle = n_e \frac{4\sqrt{2\pi}}{3} \Big( \frac{Ze^2}{4\pi\epsilon_0} \Big)^2 \frac{ln\Lambda_e}{\sqrt{m_e (k_b T_e)^3}} \tag{1.16}$$

where $ln\Lambda_e$ is the Coulomb logarithm, considering that $v_e = \sqrt{k_b T_e / m_e}$
In the last contribution, it can be noticed that $\nu_{ei}^{(p)} \propto T^{-3/2}$.
An important parameter for inductively coupled plasmas is the *Skin Effect*: in a conductor, the alternating electric current is mainly distributed between the surface and a level named *skin depth*, that depends on physical properties and frequency. Finally, according to [13], It can be found that the power transferred to the plasma can be expressed as:

$$P_{plasma} = \frac{e^2 E_0^2 n_e \delta}{4 m_e} \frac{\nu_c}{\nu_c^2 + \omega^2} \tag{1.17}$$

where $\omega$ is the RF pulsation and $E_0$ the induced electrical field.
The second process which contributes to plasma heating is called collisionless, stochastic, nonlocal or anomalous heating [13]. Due to the spatial variation in the skin depth layer, the time varying electric field which acts on an electron is nonperiodic and the particle can lose phase coherence with the field (strictly periodic), thus producing stochastic interaction with field and collisionless heating. [13]

### 1.3.2 Negative Ion Production

Negative ions are produced in an ion source by two main processes:

- *Volume production*: This process take place inside the plasma and it can be divided into two steps [3] [6].
  First, hydrogen molecules are vibrationally excited by collisions with "fast" electrons ($E_e > 20eV$)

$$H_2 + e_{fast} \rightarrow H_2^* + e \tag{1.18}$$

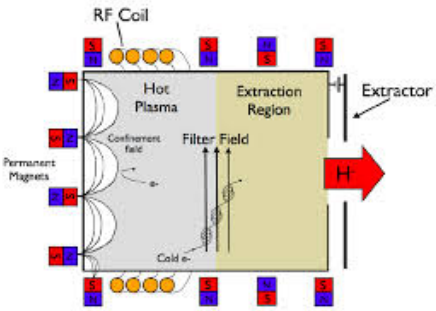


Figure 1.7: Negative ion source. The presence of two zones separated by the filter field can be noticed

Then, negative ions are produced by dissociative attachment between vibrationally excited hydrogen molecules and "cold" electrons ($E_e < 2eV$):

$$H_2^* + e_{slow} \rightarrow H^- + H^0 \tag{1.19}$$

The first process has higher cross section for highly excited vibrational stases ($\nu > 7$) and high electron energies. However, the negative ions produced during the second process can be easily destroyed by interactions with electrons with temperatures higher than 2 eV. The main processes leading to the neutralisation of $H^-$ are:

- Electron Detachment:
$$H^- + e \rightarrow H^0 + 2e \tag{1.20}$$
- Mutual neutralization:
$$H^- + H^+ \rightarrow 2H^0 \tag{1.21}$$
- Associative detachment:
$$H^- + H^0 \rightarrow H_2 + e \tag{1.22}$$

The dominant process at temperature above 1eV is the electron detachment. To reduce the $H^-$ losses, the source is divided into two parts: a hotter region, named *driver*, where the main plasma heating is located and hot electrons produce excited molecules and a colder region, named *extraction zone*, where negative ions are produced. There are two methods to cool the plasma: the first consists in the expansion of the source volume in the extraction zone, while the second employs a transverse magnetic filter field, which prevents hot electrons from accessing the extraction zone, due to their lower collisionality. [10]

- *Surface production*: It has been demonstrated that the injection of caesium vapor in the source causes a 3-10 times enhancement of negative ion production[6]. Caesium produces a thin layer over the wall surface, thus causing a lowering of the work function. Ion production has to be improved expecially close to the grids, where $H^-$ produced by collisions of the $H^0$ and $H^+$ on the source wall and plasma grid, can be extracted before being neutralized.

### 1.3.3 Acceleration

Once the negative ions have been produced, it is necessary to extract and to accelerate them in order to form the ion beam. The extraction system, composed by grids, is responsible for the main beam properties such as the ion current and the beam profile.
The edge between the plasma and the zone in which the electric field affects charged particles is named "*meniscus*" and it is defined as the region with potential equal to zero with respect to the source; it has the shape of a convex lens.
Since electrons have the same electrical charge as the negative ions they are extracted and accelerated too. Several techniques can be employed in order to avoid the acceleration and reduce the extraction of electrons: first of all, the first grid, generally named Plasma Grid, can be biased positively (10 - 20 V) with respect to the source body. The effect is higher by introducing an additional plate, named *Bias Plate* in front of the plasma grid. It is electrically connected to the source walls and it decreases the biased area by extending the source potential near the apertures. [7] Moreover, once electrons are extracted by the potential difference between the first two grids they are deflected by magnetic fields. The extracted current can be

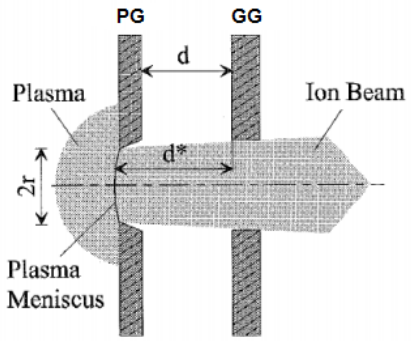


Figure 1.8: Beam extraction in a two-grid system.

determined using the Child-Langmuir equation [5], which describes the trend of the current as a function of the extraction voltage. Because of the "space charge limited current condition", it is supposed that the current can not increase endlessly, due to the repulsion of the charge particles. Using a plane diode model and assuming

that the initial ion velocity is negligible, the extracted current can be written as:

$$I_{ex}^{max} = \frac{4}{9}\pi\epsilon_0\sqrt{\frac{2e}{m}}\left(\frac{r}{d}\right)^2 V_{ex}^{3/2} \equiv \Pi_0 V_{ex}^{3/2} \tag{1.23}$$

where $r$ is the radius of grid openings, $d$ the distance between grids and $m$ the mass of the charged particle.
However, in ion beam operation the distance $d$ has to be substituted by the distance between the extraction grid and the meniscus, $d^\star$. A fundamental parameter to describe the beam optics is the normalised perveance, defined by:

$$\Pi = \frac{I_{ex}}{V_{ex}^{3/2}} \tag{1.24}$$

this parameter is used because of its relation with the beam divergence. Assuming that the angle distribution between the beam axis and the beam particles velocity vector after the extraction follow a Gaussian trend with a standard deviation $\sigma$, the divergence angle is defined as

$$\epsilon = \sqrt{2}\sigma$$

In a three-grids system, in which an Extraction Grid (EG) is placed between the Plasma Grid and the Grounded Grid, the divergence depends not only on the perveance but also on the ratio between the acceleration and the extraction voltages.

$$\epsilon = \epsilon\left(\frac{\Pi}{\Pi_0}, \frac{V_{ex}}{V_{acc}}\right) \tag{1.25}$$

The optimal normalised perveance condition corresponds to the value that minimizes the beam divergence and it is experimentally found by measuring the divergence dipendence of $\Pi$. During the experiment, when $\Pi/\Pi_0$ is increased and the divergence first decreases (*under-perveant region*), until the minimum value is reached; then, it increases again (*over-perveant region*).
Nowadays, accelerator such as BATMAN, ELISE and SPIDER are equipped with a three-grid system. It has to be noticed that the accelerated current can not be described by equation 1.23, since this equation in obtained assuming that the initial ion velocity is negligible with respect to the acceleration. In a three-grid system is necessary to introduce modified Child-Langmuir equations, in which it is considered that ions between the EG and the GG have a non-zero velocity, being accelerated by the difference of potential between the PG and the EG. [8] , [9]
However, if it necessary to reach higher voltage than 100 kV, a the three-grid system is no more reliable. For this reason, multi-stage systems have been foreseen, in which additional grids ("intermediate grids") are used to reduce breakdown problems and to provide the capability of electrostatic focusing. [2]. A scheme of a multi-stage accelerator is reported in figure 1.9.

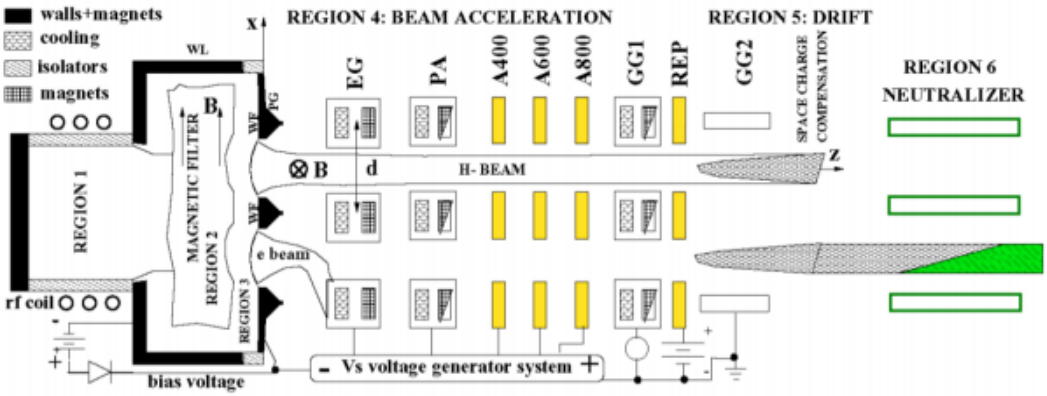


Figure 1.9: Multi-stage acceleration system

Before being injected inside a TOKAMAK, the negative ion beam must be neutralized. As can be seen in figure 1.9, after the acceleration system a neutralizer is present: in this region, negative particles ceded electrons to the neutral background gas. Moreover, deflection magnets are present, after the neutralization zone, to prevent charge particle to enter in the TOKAMAK by deflecting them on a residual ion dump, otherwise they would be deflected by the strong magnetic field.

## Aims of the thesis

This thesis provides a first characterization of NIO1 negative ion beams. Electrical measurements were used to demostrate their reliability in order to use them for the operation of SPIDER, the full-size negative ion source for ITER NBIs. In fact presently, currents on the CFC tile and on the grounded grid are not measured in main negative ion beam experiments. Comparison with spectroscopy or thermography will be performed when possible.
Because of the intrinsic plasma nature, it is not possible to obtain the same beam values during different experimental sessions. Electrical measurements, per se, are precise and their error is about 1%, but the intrinsic variability of plasmas results in an estimated confidence level of about 20 %. Therefore, the work on this thesis is focused mainly on beam trends, than on precise measurements.

# Chapter 2

# NIO1 experiment

NIO1 (Negative Ion Optimizer 1) is a small RF inductively coupled plasma source, developed at Consorzio RFX with the collaboration of the Istituto Nazionale di Fisica Nucleare in the framework of MITICA project, as a beam test facility for diagnostic systems, numerical codes and personnel training. NIO1 (figure 2.1) can extract 130 mA of negative hydrogen ions, divided into nine beamlets accelerated at 60 keV. [15]

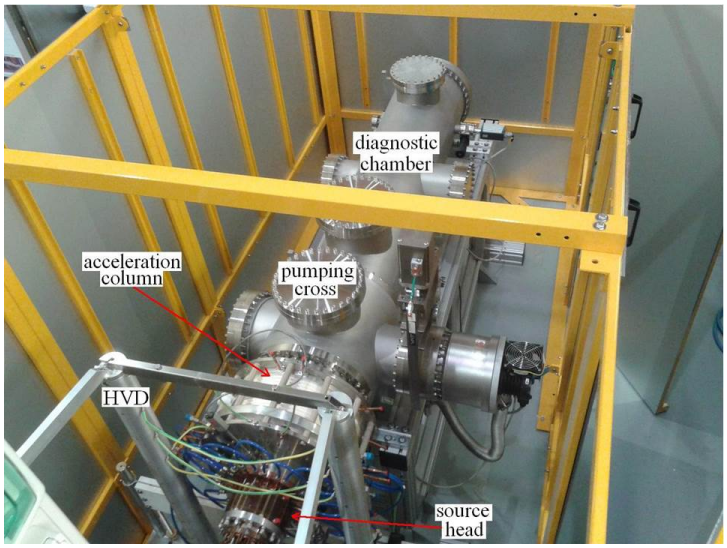


Figure 2.1: NIO1 experiment.

Nowadays, the total extracted current is lower than the expected one: a summary of achieved ion current is reported in figure 2.2

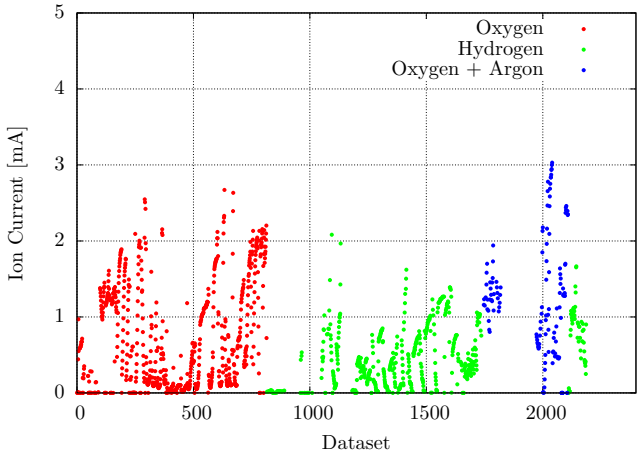


Figure 2.2: Summary of all NIO1 operations. "Ion Current" is the current collected on the PA and on the CFC tile.

## 2.1 Description of the experimental apparatus

NIO1, see figure 2.3, can be divided into three main components:

- *The source*: where an inductively coupled plasma is created by an RF generator
- *The accelerator*: a three grids system provide to extract and to accelerate the negative ion beam
- *The diagnostic tube*: where the extracted beam is studied by several diagnostic system.

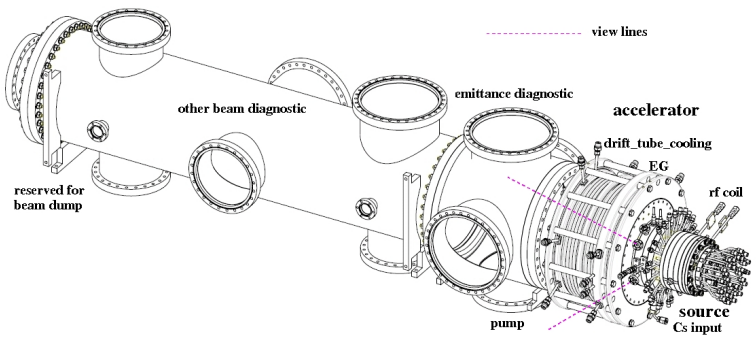


Figure 2.3: NIO1 sketch.

The source is composed by disk assemblies sealed by O-rings, producing a cylindrical chamber with 5 cm radius in which the plasma is generated through inductive

coupling and confined by a multipole magnetic field. It is created by permanent magnets placed on source walls that produce a minimum B magnetic bottle. The RF power is coupled to the plasma through a seven turn copper coil encased in polysulfone shells (figure 2.4) .

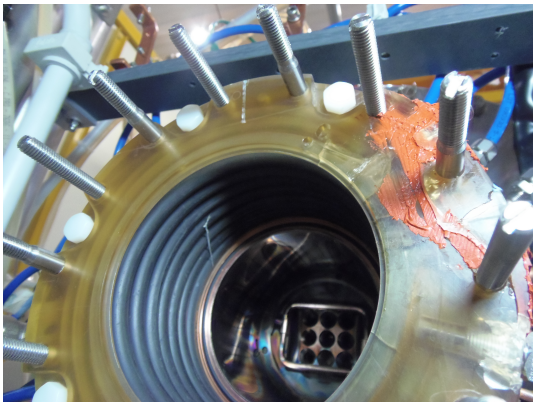

Figure 2.4: RF coil used in NIO1. The plasma grid and the bias plate are visible.

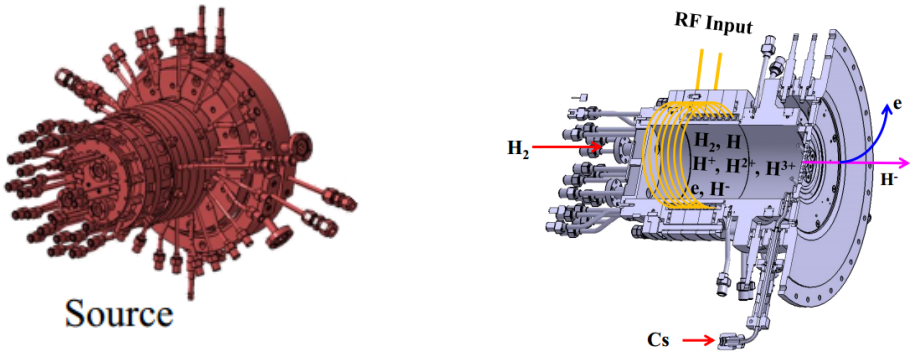


Figure 2.5: Sketches of NIO1 source.

The source is provided with vacuum windows, of which four are placed 26 mm before the plasma grid, with line of sight (LOS) parallel to it and four are placed in the back side, with LOS parallel to the beam propagation direction. Further apertures are present for the gas inlet, where the pressure gauge is connected, and to allow caesium injection. A sketch of the source can be seen in figure 2.5.
The accelerator is composed by four grids, as shown in the same figure. The *Bias Plate* is placed just before the first grid of the acceleration system; it is composed of two elements, a rectangular frame named "*Magnetic Bias Plate ($BP_m$)*" and a round frame exposed to the plasma which is referred as "Electrostatic Bias Plate ($BP_e$)". In order to improve the extraction performances, the properties of the plasma in the

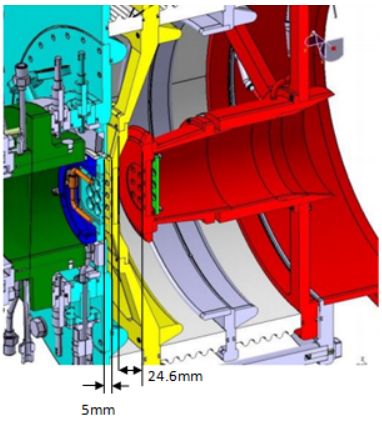


(a) Grids present in NIO1 experiment.

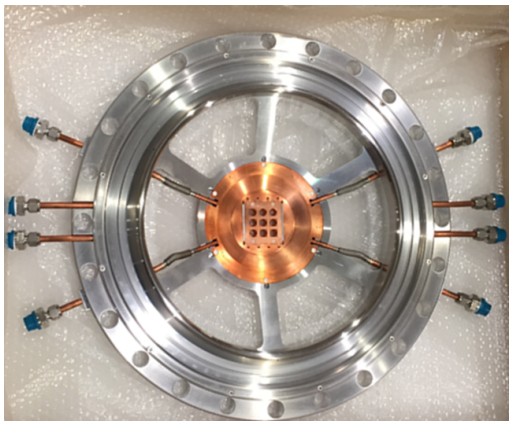

(b) Grids present in NIO1 experiment.

Figure 2.6

source can be modified by applying an electric or a magnetic field, in order to:

- keep the electronic temperature low in the extraction zone to avoid the destruction of negative ions due to stripping reactions;
- lowering the amount of co-extracted electrons.

This can be achieved by creating a magnetic filter field or by biassing positively the source with respect to the source body; in this way electrons are collected on the PG instead of enter in the accelerator. Plasma grid filter and Bias Plate have been tested with several different electrical configurations, of which a summary is present in the Appendix A. The intensity of the magnetic filter field used in NIO1 can ben seen in figure 2.7.

The acceleration column is divided into four grids (figure 2.6a), fed at increasing potential in order to extract negative particles. All have nine openings, with 3.8 mm radius, displaced in a $3 \times 3$ matrix and the distance between the centre of each hole is 14 mm.
Starting from the source, we find:

- *Plasma Grid (PG):* It faces the plasma. It can reach -60kV with respect to the ground. Moreover, in order to reduce electron extraction, it can be biased up to 20 V with respect to the body source.
- *Extraction Grid (EG):* It held higher voltage than the PG voltage to extract and accelerate ions. It can reach about -52 kV and the voltage can be tuned to optimize beam optics. Four permanent dump the extracted electrons on the EG itself.
- *Post Acceleration Grid (PA):* It coincides with the grounded grid.

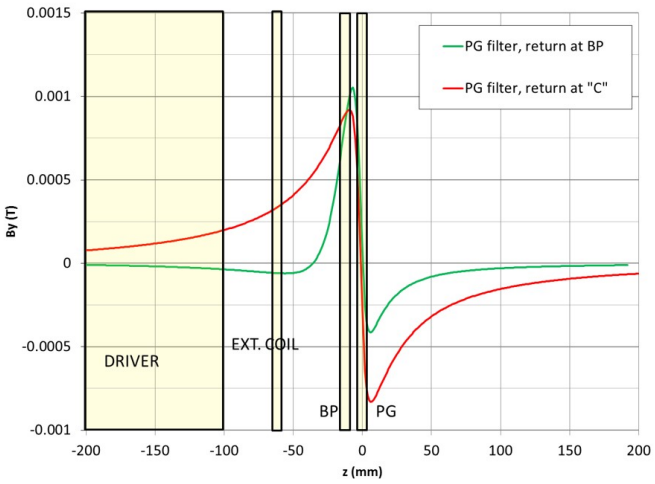


Figure 2.7: Magnetic filter field simulations produced by the two different circuits used in NIO1.

- *Repeller electrode* it is placed after the PA and it is bias to positive voltages to prevents positive ions to be accelerated back in the source.

All grids are water cooled to prevent damages caused by heat produced by impacting particles.
The diagnostic tube, is made of a metallic tube (length = 1.5 m and inner diameter= 350 mm) in which several view ports are present, hosting different diagnostics. Two turbomulecolar pumps and scroll pumps are connected through cross-pumps in order to reduce the pressure in this zone and the consequent stripping losses. The vessel pressure is controlled by a dual pressure gauge, able to work as a Pirani or as a ionization.

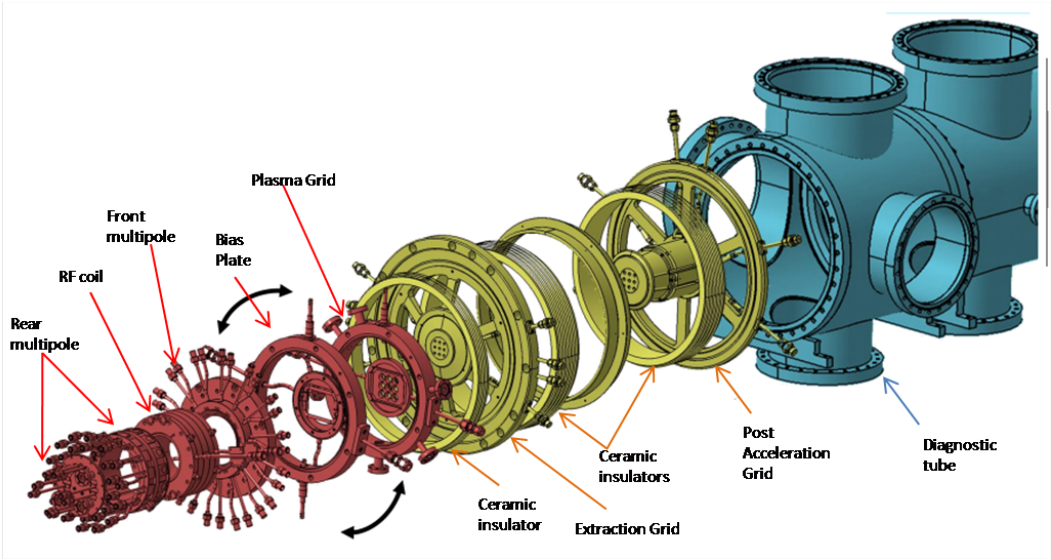


Figure 2.8: Expanded scheme of NIO1 components. THe source in red, the accelerator in yellow and the diagnostic tube in light blue.

## 2.2 Diagnostic systems

Several diagnostic systems are foreseen in NIO1 to provide a full characterization of source and beam and also to test them for future *SPIDER* and *MITICA* applications. Nowadays, only a portion of the expected diagnostics has been installed. Here a short brief of all diagnostic systems.

- **Optical Emission Spectroscopy (OES)**: The radiation spontaneously emitted by the plasma source and by the extracted beam yields a great variety of plasma parameters, such as electron temperature and density, neutral hydrogen and caesium density. The presence of impurities in the plasma and the isolated Balmer series lines can be monitored with a low resolution spectrometer. In NIO1 a 16 bit *Hamamatsu* mini spectrometer TM series C10082CAH is used, with 1 nm resolution and capable to measure a spectrum between 350 and 850 nm.
  However, rotational and vibrational molecular spectra need an high resolution spectrometer: for this purpose, a Czerny-Turner spectrometer is used; it has a spectral resolution of 0.05 nm, it can work between 350 and 1300 nm but it is capable to acquire a spectral range of only $5 - 6$ nm. [17]

- **Plasma Light Detection (PLD)**: This diagnostic is based on the fast response of a photodiode. It is useful to detect plasma switching on and off, its transition from the capacitive coupling mode to the inductive coupling mode and it can also be used for studying fast plasma dynamics. Presently, optical

fibre carries the signal to an Hamamatsu photomultiplier, model H107222.

- **Luxmeter**: It is employed to measure the photons emitted by the plasma in the source

- **Beam Emission Spectroscopy (BES)**: It is based on the interaction between the energetic ions and the molecules of the background gas present in the vacuum chamber. These collsions produce excited neutral atoms that emit photons.
  The most intense emitted radiation corresponds to $H_\alpha/D_\alpha$ transition (n = 3 to n = 2). In the laboratory frame of reference, the emitted radiation wavelenght is shifted as described by relativistic Doppler effect:

$$\lambda' = \lambda_0 \frac{1 - \beta cos\alpha}{\sqrt{1 - \beta^2}} \tag{2.1}$$

  where $\lambda'$ and $\lambda_0$ (656.2 nm) are respectively the measured and the unshifted wavelenghts, $\beta$ it the ratio between the speed on ion and the speed on light and $\alpha$ is the angle between the de-excite beam direction and the observation direction. [18]

- **Cavity Ring Down spectroscopy**: it allows the measurements of the negative ion density inside the source through the photodetachment process. CRDS consists of two highly reflective plano-concave mirrors, installed on two collinear vacuum windows and in a laser pulse forced to bounce between the mirrors several times. The laser pulse is gradually absorbed by negative ions and comparing the absorbtion with and without the plasma, the negative ion density can be obtained. CRDS will be able to measure the density of negative ions behind the PG in a range between $10^{14}$ and $10^{17}$ $m^{-3}$.

- **Fast Emittance Scanner**: It allows the measurements of the beam particle distribution in the 6D phase space. In NIO1 an Alison scanner will be used and it will be placed in the crossing ports at 0.46 m from the PG, with the possibily to use it either horizontally or vertically.

- **Visible Tomography**: It will measure the beam density profile through the $H_\alpha$ emission. The measurement corresponds to the line integral of the beam emitted radiation, therefore an inversion algorithm is necessary to obtain the 2D map of the density. It will be based on two linear CCD cameras mounted in two orthogonally viewing ports of the diagnostic chamber.

- **Calorimeter**: It consists of a copper plate target, with 13 tubes that continue out of the plate to the front lid. Thermocouples are installed in these tube sections and insulated by kapton.
  The beam intensity profile, along the direction perpendicular to the tubes,

can be obtained by their temperature variation. Moreover, the rotation of the calorimer by 90° can yield a 2D beam intensity profile. Presently, the static calorimeter has not been implemented yet and a CFC tile is used.

- **Mini-STRIKE**: This diagnostic system is made of a Composite Carbon Fiber (CFC) tile, with dimension of $120 \times 90 \times 12$ mm, whose Thermal conductivity is anisotropic: heat flux along the direction perpendicular to the beam propagates 20 times faster than in the other directions. It is used to measure beam divergence, beam profile and the beam current after the repeller electrode. Beam profile and divergence are obtained by a thermocamera that records the rear side of the tile.
  Prototype tiles has been employed at IPP since 2012 and it was verified that they can investigate beam properties on beamleats scale. [19] A smaller tile (STRIKE) will be employed in SPIDER.

- **Thermoclouples:** A lot of facing plasma components are water cooled, such as grids and the source. It is possible to measure the temperature difference between inlet and outlet water of each cooling circuit: this difference is proportional to the power ceded by plasma to components. For example, five thermocouples are placed in the source: four of them in the front multi-pole and the other in the rear multi-pole. Thermocouples not have diagnostic purposes only; they are also used to control the temperature in order to avoid damages. Presently, eight thermocouples have been installed on NIO1.

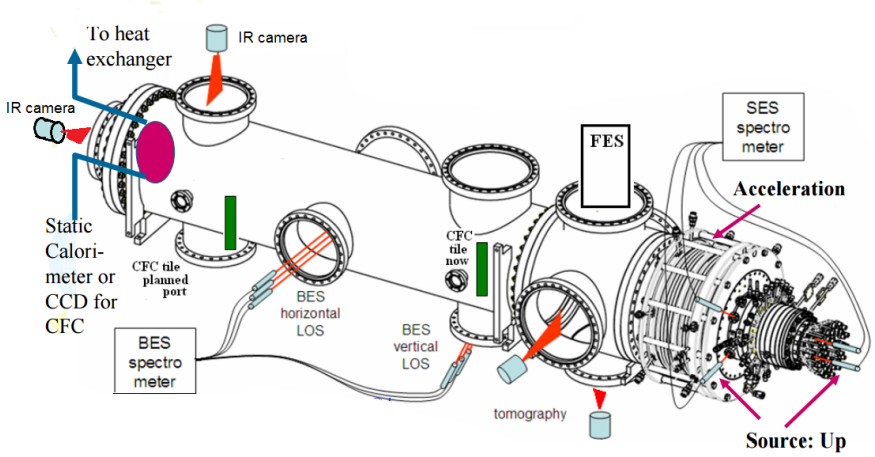


Figure 2.9: Skecth representing the diagnostic systems of NIO1

## 2.3 Database and Raspberry calibration

Experimental data are continuously recorded through an MDSplus system with an acquisition rate of 100 Samples/s. Because of large dead times present in these first experimental operations another acquisition data system is used at the same time: the operator has the possibility to save in a .csv file and in a database the acquired dataset, that can be loaded through SQL queries. In this way, useless data are reduced and a more faster analysis can be performed. In the first part of the thesis, some macros were developed in order to have a faster and an easier method to load data; macros allow to select measures in a date and dataset range. Once they have been loaded, it is possible to operate a preselection over all parameters in order to obtain only needed data [20].

During these work, except for spectroscopy measurements, only electrical data were used. These data are yielded by power supplies and then recorded in the database. The currents on the PA, repeller and CFC tile are measured by a multimeter that yields the measure of the voltage difference on a known shunt resistance. The operator reads the results and inserts them on the database manually.

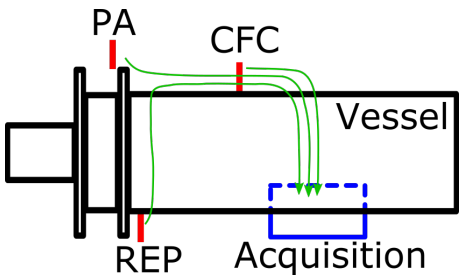


Figure 2.10: Sketch of the acquisition system.

In order to register them digitally, a Raspberry-based acquisition system was implemented (figures 2.10 and 2.11).
The voltage signal is converted by the raspberry in "raw data", expressed in bit from a minimum of 0 bit (-1.6 V) to a maximum of 4095 bit (1.6 V). Using the conversion formula given by datasheet [21] and including in it the shunt resistance, a current value is obtained.

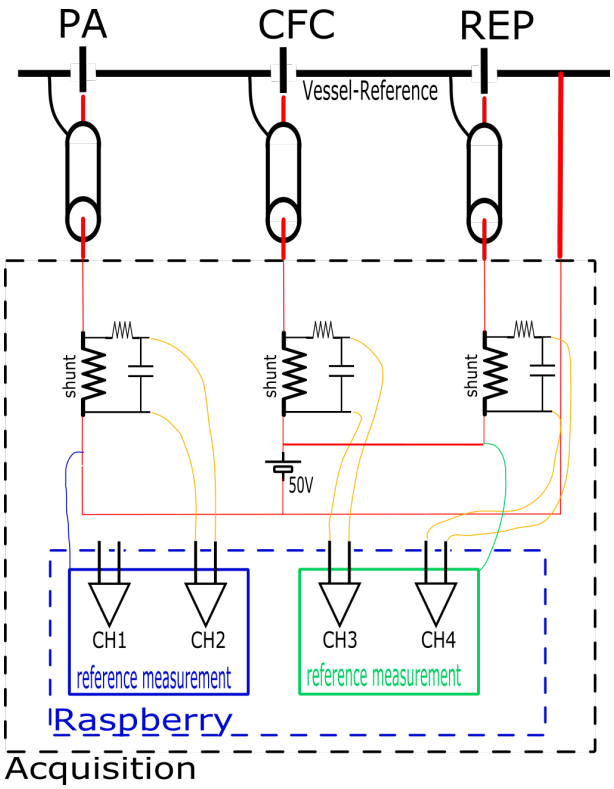


Figure 2.11: Sketch of the raspberry electrical scheme.

# Chapter 3

# Oxygen operations

Nowadays, negative ion production in NIO1 experiment is low for two main reasons: first, the maximum of power supply (2500 W) has not been achieved yet; during present operations the RF power supply is set to a maximum of 1000 W. Second, the negative ion production is limited by the less efficient volume production, since caesium vapor injection, is not yet available in NIO1. This results in an extracted current of only few mA current. In order to increase the extracted current and be able to test the acceleration system, a number of experiments was performed using oxygen as a working gas: it has higher electronegativity than hydrogen, thus reducing the ion destruction caused by electron detachment. Also due to the higher oxygen mass, ions are less affected by magnetic fields in the source and for this reason are easier extracted even at low extraction voltages. Moreover it allows to obtain a more collimated beam with respect to that generated using hydrogen it reduces also the deflection caused by permanent EG magnets, as can be seen by simulations (figure 3.1).

It was experimentally observed that oxygen requires less RF power with respect to hydrogen to switch to the inductive coupling: the transition happens at 400 W, against the 900 W required by hydrogen.

In this chapter, the main oxygen operation results will be exposed, starting from the electrical measurements on the EG in section 3.2, where the effects of filter and source bias on the co-extracted electrons are treated. In section 3.3, beam current measurements on the PA and the CFC tile will be discussed, trying to assess the best operational conditions, by considering the effects of the soure pressure, the RF input power and also by the acceleration voltage. The effect of the magnetic filter field and of the source bias will be discussed.

During the latest experimental campaignes, a mixture of oxygen with a 10 % of argon was used since from a selection of argon emission lines the electronic temperature and density can be obtained. Extraction operations are not affected by the argon doping; being a noble gas, it is difficult to positively ionize. The creation of argon negative ions is possible only by providing energy; produced ions are metastable and

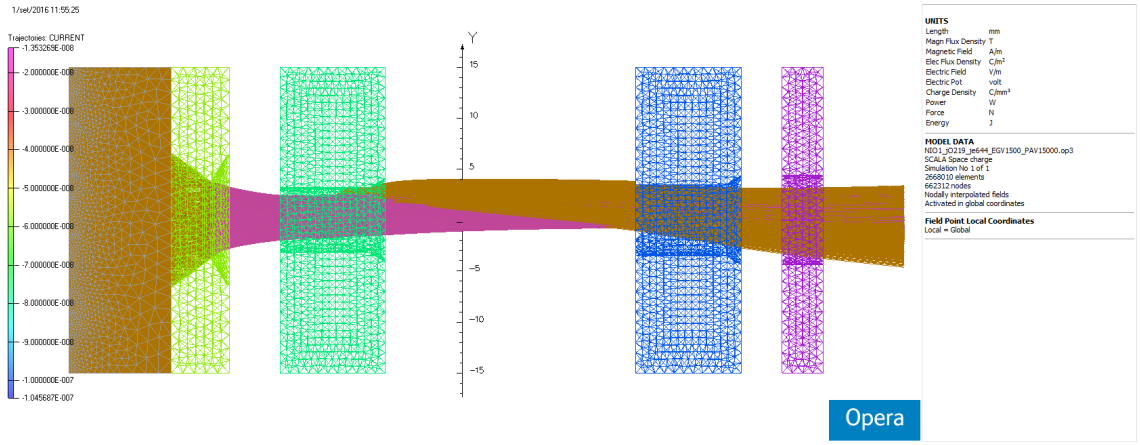


Figure 3.1: Oyxgen beam (purple) and hydrogen beam (brown). The greater deflection of the second beam can be noticed, in the same magnetic field produced by EG magnets

they quickly lose the electrons.
In the latest experimental days, a new magnetic circuit was installed (see Appendix A). The main analysis will be carried out using the data acquired with the old magnetic circuit. However a comparison between the two different configuration will be done.

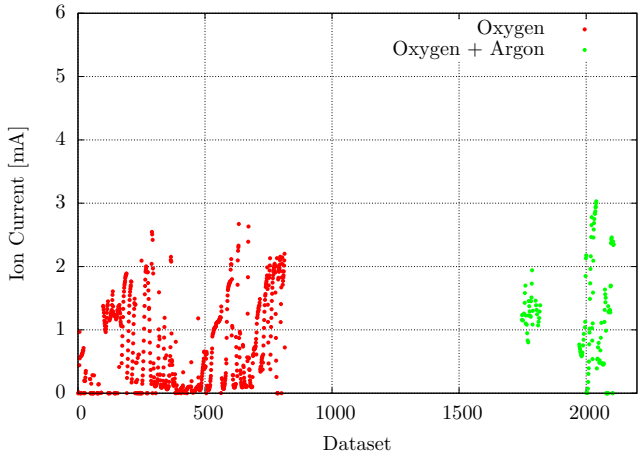


Figure 3.2: Summary of the oxygen operation. "Ion Current" is the current collected on the PA and on the CFC tile.

## 3.1 Reflected Power

The reflected power is the component that can not reach the coil and it returns back to the generator. Coils, matching box and trasmission line constitute the primary circuit coupled to secondary, constituted by the plasma; A full treatment can be found in [12]. The reflected power reaches its minimum when the load impedance is equal to the resonant impedance, $Z_0 = 50\Omega$. By varying source parameters, such as pressure, input power or filter field current, a change in the reflected power was observed, since these parameters changes the plasma impedance, which contributes to the load impedance. In oxygen operations, the lowest relative reflected power was found at 600 W; with larger RF power, higher reflected power was observed. Moreover, when the plasma is not in inductive regime, the reflected power is high, but it abruptly decreases when the transistion happens. It has been speculate the possibility of using this parameter to determine information about the electronic density in NIO1, as proposed in [24]. In Appendix B, an alternative method to obtain the electronic density starting from the reflected power is proposed, since in NIO1 voltages and currents at the coil are not presently available this method can not be applied, but it would be the subject of future works.

## 3.2 Electron Current

The extraction voltage is the difference between the voltage on the PG and the EG and this difference will be referred to as "EG voltage". It controls the extracted current; both ions and electrons are extracted but the latter are deflected onto the EG by permanent magnets housed in the EG itself; these electrons form a current which is measured and named so far "EG current" or "electronic current". In this section the EG current will be studied in different source conditions. It is expected that all co-extracted electrons are deflected onto the EG, despite value of the acceleration voltage. Next figures (in particular figures 3.3a and 3.4a) show that the current on the EG is mainly influenced by input power, source pressure and extraction voltage. The study of the electronic current is fundamental in order to optimize NIO1 operations; in particular a decrease of co-extracted electrons is auspicable for several reasons. First because, the EG power supply is set to hold a maximum current of 600 mA in order to avoid grid damages. Second, both ions and electrons are extracted: since for each extraction voltage a maximum extract current exists, the lower the electrons, the higher the possibility of extracting ions. MITICA has to demonstrate the capability to obtain a ratio between the co-extracted electronic current and extracted ion current is prescribed to be lower than one; finding on NIO1 in which conditions this ratio value can be obtained will be useful for addressing MITICA optimization. This last hypothesis will be further discussed in subsections 3.2.2 and 3.3.3

### 3.2.1 RF input power and source pressure

RF power and source pressure are the main parameters on which the operator can act in order to change plasma properties. By increasing input power, more energy is transferred to the plasma particles, while by enhancing the pressure higher collision frequency is obtained. In this subsection, the filter field current and the source bias are kept constant and their values indicated.
The first interesting results are those referred to the EG voltage - current characteristic curve where a confirmation of the Child - Langmuir law was expected (equation 1.23).

It resulted instead that the law is verified only at very low EG voltages (figures 3.3b and 3.4b), while at higher voltages a linear trend is instead found (figures 3.3a and 3.4a). A possible explanation refers to the plane diode model, introduced in section 1.3.3. In this model electrons are emitted by an electrode due to thermoionic effect. However, the extracted current can not grow endlessly, since there exists a voltage limit beyond which the electrode can not emit further electrons. This limit is given by the Richardson Law. Similarly, it can be expected that a limit exists also for the plasma facing the plasma grid. For low extraction voltages, only particles in the meniscus zone are extracted and the current is determined by the Child-Langmuir Law. Once all these negative particles have been extracted, a flux from the inner source region to the PG is necessary induced in order to keep the neutrality in the meniscus zone. These particles are therefore extracted with a non-zero velocity and equation 1.23 is no longer valid.
EG voltage-current characteristic curves were obtained by fixing input power (figure 3.3a) or source pressure (figure 3.4a) and by varying the other parameters. Considering first figure 3.3a, it can be seen that all the characteristic curves have the same trend and the extracted electron currents are comparable as a function of pressure, with the exception of the scan performed at 0.07 Pa. This can be seen also in figure 3.5, where data of figure 3.3a are reported against the source pressure instead. Above 0.2 Pa EG current stays constant and does not depend on source pressure.
Figure 3.4a, shows that the input power influences electronic currents. In the considered pressure and RF power ranges, it can be concluded that pressure and input power act in different ways on gas ionization. These considerations need to be confirmed in future operations, when the maximum input power limit will be reached.

Linear portions in previous images have been interpolated with linear functions $f(x) = ax + b$ and results are reported in tables 3.1 and 3.2. In table 3.1 both slopes and intercept increase by enhancing the input RF power. The increasing of the intercept value is a further confirmation about previously performed simulations [12], where it was found that the electronic density grows as a function of the input power. In fact, it is expected to produce higher ionized plasma by increasing the in-

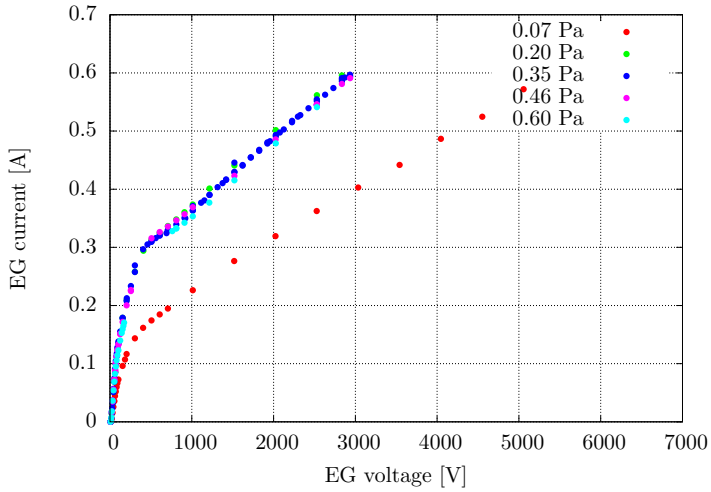


(a) EG current as a function of EG voltage, at different source pressure. 1000 W RF input power, 300 A filter, 10 V bias.

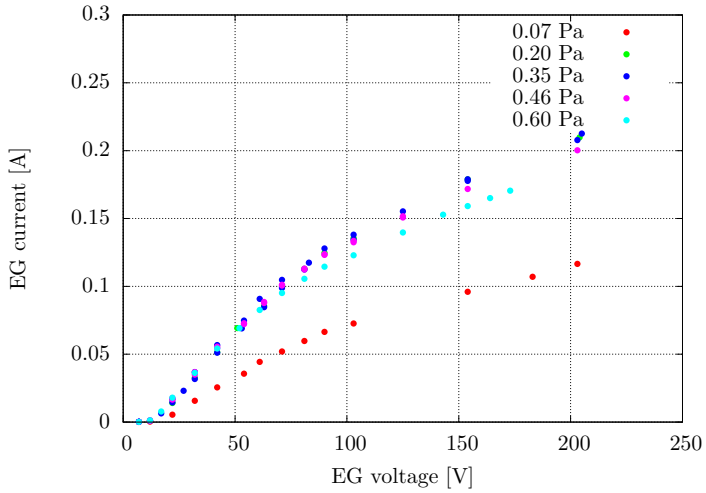


(b) Zoom on lower voltage. The Child-Langmuir law trend can be recognised for very low voltages.

Figure 3.3

put power, which obviously yields higher electronic density, thus allowing to extract more electrons. The different dependence of input power or pressure on plasma can be seen also by these results: in the first table both slopes and intercept increase by enhancing the power, while in the second table slopes corresponding to pressures equal or higher than 0.20 Pa are comparable. Pressure scans should be performed in order to find a range in which, at fixed extraction voltages, the extracted current

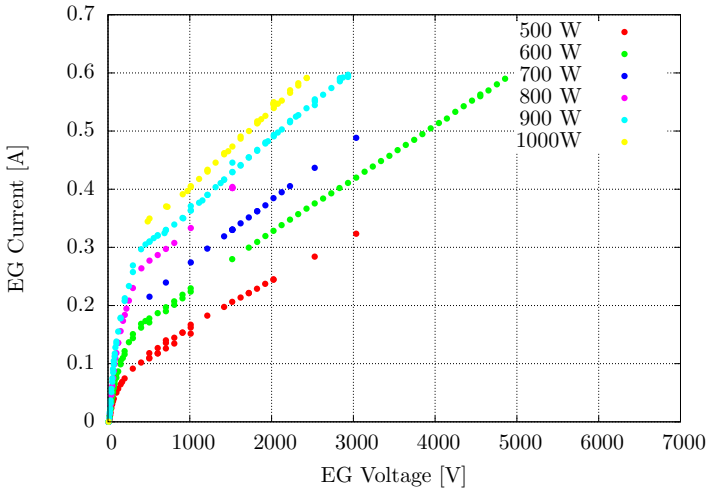


(a) EG current as a function of EG voltage, at different input power. 0.35 Pa source pressure, 300 A filter, 10 V bias

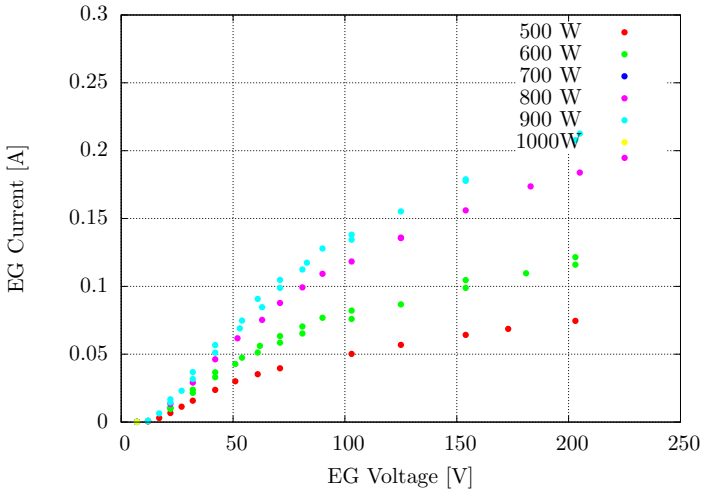


(b) Zoom on lower voltage. The Child-Langmuir law trend can be recognised for very low voltages.

Figure 3.4

assumes a descending trend as a function of the pressure.

Scans reported in figure 3.4a revealed an unexpected phenomenon: during operations at source pressure equal to 0.46 Pa and 0.60 Pa, the electron current on the extraction grid abruptly reaches the maximum value allowed by the EG power supply (600 mA), this for particular EG voltages. This problem has been solved by

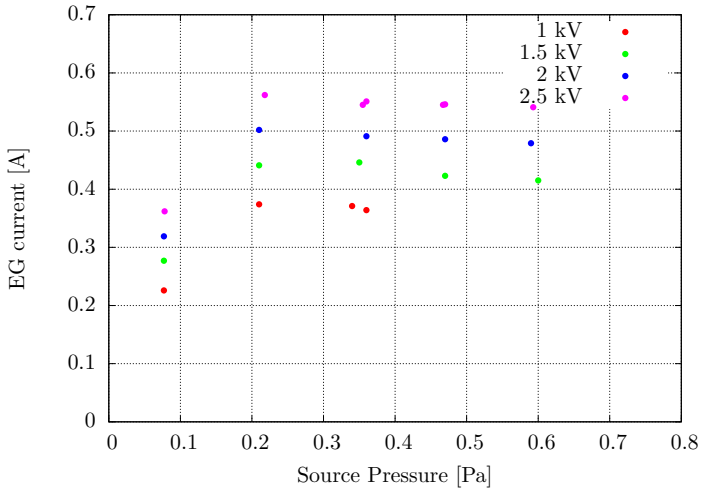


Figure 3.5:

| Source Pressure(Pa) | a ($\times 10^{-5}$ A/V) | b (A) |
|---|---|---|
| 0.07 | $9.36 \pm 0.17$ | $0.129 \pm 0.002$ |
| 0.20 | $12.29 \pm 0.08$ | $0.250 \pm 0.001$ |
| 0.35 | $12.06 \pm 0.06$ | $0.245 \pm 0.012$ |
| 0.46 | $11.48 \pm 0.06$ | $0.254 \pm 0.001$ |
| 0.6 | $12.48 \pm 0.05$ | $0.227 \pm 0.001$ |

Table 3.1: Linear fit

| Input Power (W) | a ($\times 10^{-5}$ A/V) | b (A) |
|---|---|---|
| 500W | $8.65 \pm 0.16$ | $0.071 \pm 0.002$ |
| 600W | $9.87 \pm 0.08$ | $0.126 \pm 0.014$ |
| 700W | $10.92 \pm 0.06$ | $0.163 \pm 0.011$ |
| 900W | $12.06 \pm 0.06$ | $0.245 \pm 0.012$ |
| 1000W | $13.34 \pm 0.11$ | $0.271 \pm 0.019$ |

Table 3.2: Linear fit

decreasing the pressure, and increasing the EG voltage. Then, the source pressure was returned to the initial value. In figure 3.6 scans at 0.46 and 0.60 Pa are reported and the forbidden zone can be seen.

| Source Pressure | Forbidden Zone |
|---|---|
| 0.40 Pa | $200 - 480$ V |
| 0.60 Pa | $160 - 760$ V |

Table 3.3: Forbidden zone range as a function of the pressure

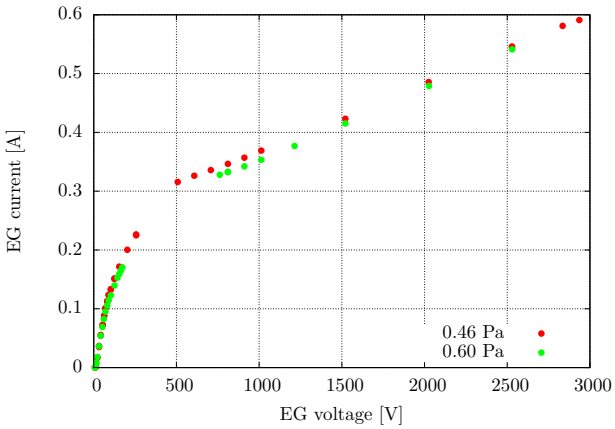


Figure 3.6: Forbidden zone for two different pressures

Outside the forbidden zone, electron currents on the EG returns to follow the trend reported in figure 3.3a. It has been supposed that this phenomenon could be caused by electrons trapped between the PG and the EG. [31]

### 3.2.2 Filter and Bias

In order to limit the electronic density and temperature in the extraction zone and to improve the negative ion density, it is possible to act on source bias and on the magnetic filter. The PG can be polarized up to 20 V with respect to the source body, thus modifying the electrostatic field in the meniscus zone and attracting electrons which are absorbed on the grid itself instead of being extracted by the voltage difference between the PG and the EG and collected on the EG itself. This is useful since extracted electronic current influences the extraction of negative ions, due to the space charge. Furthermore, the magnetic filter power supply can be changed, in order to modify the field intensity. The more intense the magnetic filter, the lower the electronic temperature in the extraction zone; higher magnetic filter field allows to increase the extracted current, since hot electrons easily destroy negative ions.
In figure 3.7 the effect of both magnetic filter and source bias can be seen: the main aim of the magnetic field is to prevent high energy electrons from diffusing into the extraction region; however it produces a decrease of the current gathered on the EG, probably due to an electronic density decrease in proximity of the meniscus.
In figure 3.7a, in which the offect of the filter field on the electronic current is

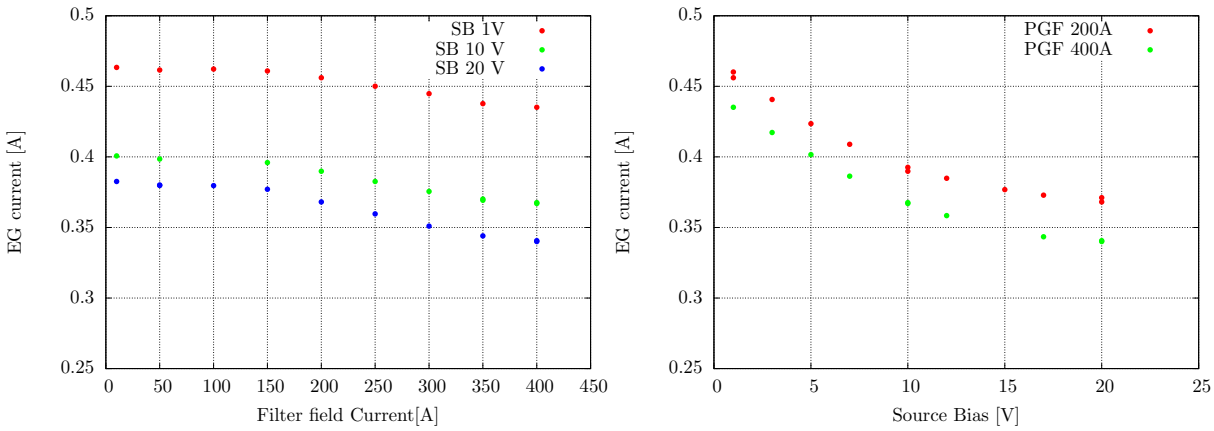


(a) (b)

Figure 3.7: 800 W, 0.35 Pa source pressure, EG voltage = 1500 V, AG voltage = 15000 V, Configuration II , PA/CFC ≈ 0.4

presented, it can be seen that a reduction of electrons is detectable over 100 A. At lower filter current, no EG current decrease was observed.

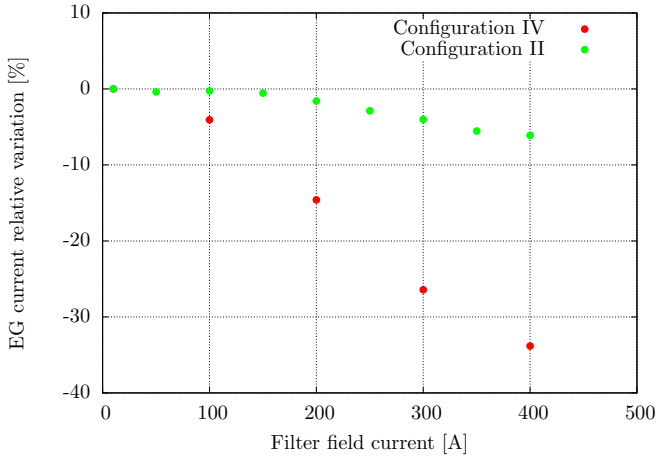


Figure 3.8: Comparison between the old magnetic circuit (in green) and the new magnetic circuit (in red). Currents have been normalized with respect to their maximum value.

In the introduction it has been said that both filter and source bias connections were changed, in order to find more efficient configuration. Scans reported in former figures were performed using configuration II, in which the old magnetic circuit was used. In this configuration, it can be seen that the electronic current is mainly reduced by acting on the source bias. In fact, as reported in the Appendix A, in this magnetic configuration, the filter field is highly localized between the plasma grid and the bias plate.
It is interesting to note that in the bias scan (figure 3.7a): the electronic current collected on the EG decreases faster between 0 and 10V than between 10 and 20 V. This could be partially explained by thinking to the Langmuir-Probe I-V characteristic curve. A brief explanation about how this diagnostic system works can be find in section 5.2. In this curve a change of trend happens above the plasma potential: the collected current at higher potentials presents a saturation trend and increases slowly. The current decrease detected on the EG is related to the current absorbed on the PG. If this current reaches the saturation level, the bias becomes less efficient to reduce co-extracted electrons.
In figure 3.8, a comparison between the reduction of co-extracted electrons produced by the two magnetic configuration is shown. The magnetic filter field produced with Configuration IV acts upon a wider region with respect to that produced in Configuration II (figure 2.7). For this reason, it is also more efficient to prevent high energy electrons from diffusing to the extraction zone.

## 3.3 Ion Current

NIO1 has been designed to extract 130 mA of negative hydrogen, however, as reported before, the creation and the extraction of oxygen negative ions is favoured by higher electronegativity and higher mass.
The extracted total ion beam is divided into the current gathered on the PA, the CFC tile and the repeller. Presently, the current gathered on the repeller has not been considered, since it was observed that it was mainly caused by other charged particles. Good operational parameters are those that maximize the CFC tile current and minimize the PA current. In fact, the latter is constituted by beam ions that are lost: the lower this currents, the better the operational efficiency, which is influenced by several factors:

- **Space charge**: As explained in section 1.3.3, the extracted current is limited by the space charge. Both ions and electrons are extracted; the latter influence the extraction of the former. Co-extracted electron current decrease has been treated in section 3.2.

- **Ion Density**:High negative ion densities are essential, but negative ions are easily destroyed by electrons with energy $> 2$ eV. The transverse magnetic field can be increased in order to confine more efficiently high energy electrons in the driver zone.

- **Beam optics**: It mainly depends on the extraction voltage even if secondary parameters exist, such as the acceleration voltage. Beam optics measurements can be obtained by analysing on the thermocamera images, but some information can be obtained also by the ratio between the current gathered on the PA and the current gathered on the CFC tile: the lower the ratio, the better the optics.
  Several EG and AG scans were performed in order to determine those conditions in which the ratio between two currents is lower. Moreover, in order to find what parameter have more influence on beam optics, RF scans, pressure scans and filter scans were performed.

- **Stripping losses**: They are caused by interactions between the negative ion beam and the background gas in the accelerator that causes the loss of the electrons and positive ions or neutrals are produced; collisions inside the accelerator produce electrons that are aboserbed on the PA, while if they occur after the acceleration zone, positive ions are then attracted to the repeller electrode. Stripping losses can be reduced by operating at lower source pressures and by increasing the pumping speed, which reduces background gas pressure in the vessel and in between the grids.

In this section several parameters which affects the total ion current will be considered, in order to provide a first beam characterization and investigate the effects that they produce on NIO1 beam. This characterization is fundamental in order to understand how the device works, the conditions in which extraction performances are optimized and to plan required upgrades.

### 3.3.1 RF input power and Source Pressure

First investigations have been devoted to assess the dependence of total ion production on source pressure and RF power. Several data have been taken keeping the acceleration voltage constant. Figures 3.9 shows how the input radiofrequency power affects the extracted ion current.

Reported data were taken at constant source pressure (0.35 Pa), with a 300 A filter and 10 V bias. It can be easily seen that the larger the input power, the larger the extracted current: in fact,the enhancement of the input power yields an electronic density increase (as confirmed by simulations and spectrosopy in chapter 5), which favours the ion creations by volume production increasing the interactions between molecular oxygen and electrons. The CFC tile current (figure 3.9a) presents a maximum current value, while total current ( PA current and CFC tile current) increase monotonically as the voltage is raised, even if a trend change appears (figure 3.9b). In figure 3.9a, it can be seen that in the first part of the curve, between 500 V and about 1200 V, the ion current follows the Child -Langmuir Law trend. However, since NIO1 possesses a three-stage acceleration system, the Child-Langmuir Law has to be modified in order to consider the effects of the acceleration voltage. A proper fitting function $I = aV^{3/2}$ was selected in order to verify this trend, where $a$ represents the product between the perveance (equation 1.24) and a corrective factor, $a = \Pi_0 \, K$. $K$ includes all corrective factors caused by the presence of a third grid, the distance of the meniscus with respect to the EG and other form factors related to the three dimensional beam nature. Fitting curves are displayed in Figure 3.10 and fit parameters are exposed in Table 3.4, in which the value of the coefficient $a$ and the maximum experimental voltage value for which the previous law preserves its validity are reported. In table 3.4 it can be seen that all the fit parameter are compatible within the errors, as it could be expected, since this equation is a function of grid parameters and ion masses. The biggest difference lies in the maximum voltage for which the theorical law is still valid. A similar trend was reported also for the electronic current (Figures 3.4a and 3.3a) and a similar explanation can be used; the law is verified until all the charged particles in the extraction zone are extracted, then particles coming from other zones of the source start to be extracted, not following the Child-Langmuir law. Because of lack of data, it is not possible to verify if the second curve part presents a linear trend as for the electronic current; this analysis will be performed when the system will be capable of withstanding higher voltages.

However, an attempt to parametrize the curve in a $V_{ext}$ range between 1200 V

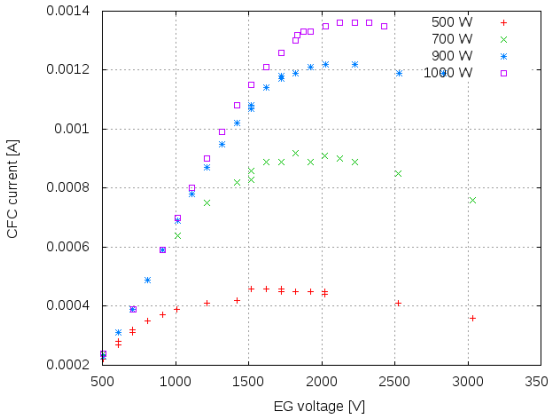


(a) CFC current as a function of the extraction voltage

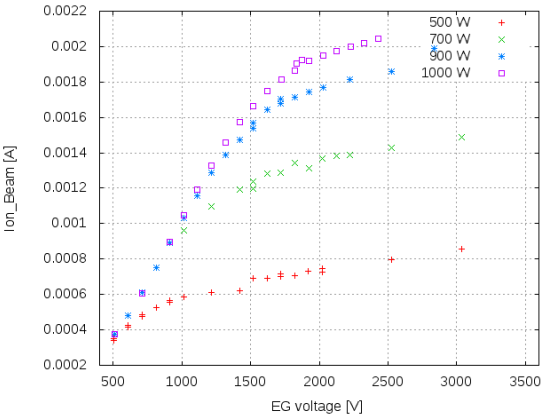


(b) CFC + PA current as a function of the extraction voltage

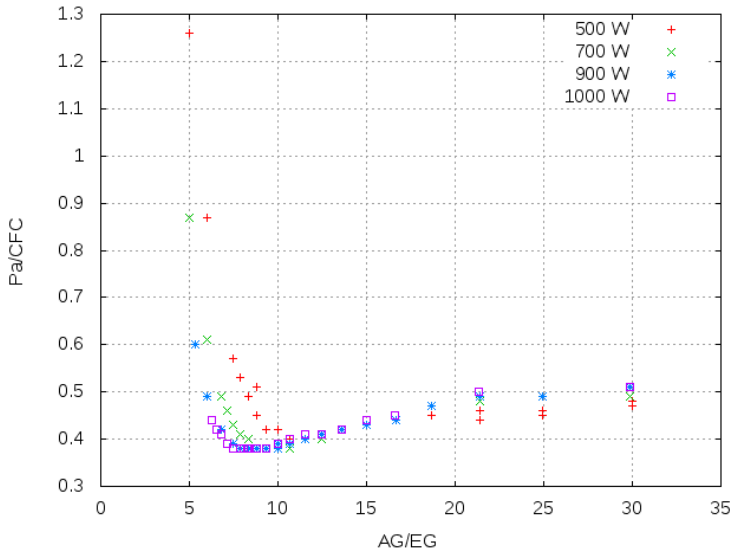


(c) Optics scan

Figure 3.9: Radiofrequency power scans. Constant source pressure (0.35 Pa), 300 A filter and 10 V bias.

to 2400 V was performed. It has been observed that plotting the normalized perveance as a function of the extraction voltage, the curve present in figure 3.11a was obtained, where two trends can distinguished. Between 500 V and 1100 V a flat value of perveance is found: in this range, the curve follows the Child-Langmuir law and this range corresponds to the one used in figure 3.10 to fit the curve $I = aV^{3/2}$. For $V_{ext}$ higher than 1200 V, the normalized perveance decreases linearly with $V_{ext}$. Remembering that $\Pi = I_{ext}/V_{ext}$ and considering that in the range between 1200

| $P_{in}$ (W) | $a \times 10^{-8}$ ($A/V^{3/2}$) | $V_{max}$ (V) |
|---|---|---|
| 500 | $3.05 \pm 0.05$ | – |
| 700 | $3.26 \pm 0.02$ | 915 |
| 900 | $3.23 \pm 0.01$ | 1015 |
| 1000 | $3.23 \pm 0.01$ | 1115 |

Table 3.4: Fitting results and the maximum voltage for which the theorical law is preserved.

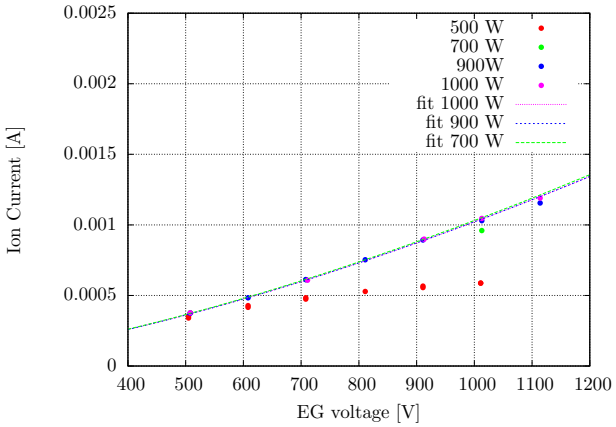


Figure 3.10: Comparison of all data trend within the range of validity.

V and 2400 V, $\Pi = -aV + b$, where $a$ and $b$ are constant, it can be found that $I_{ext} \propto -cV^{5/2} + dV^{3/2}$. Ion current data reported in figure 3.9b were fitted using the latter relation in the aforementioned range (figure 3.11b). This equation has purely descriptive aims and further investigations will be performed.

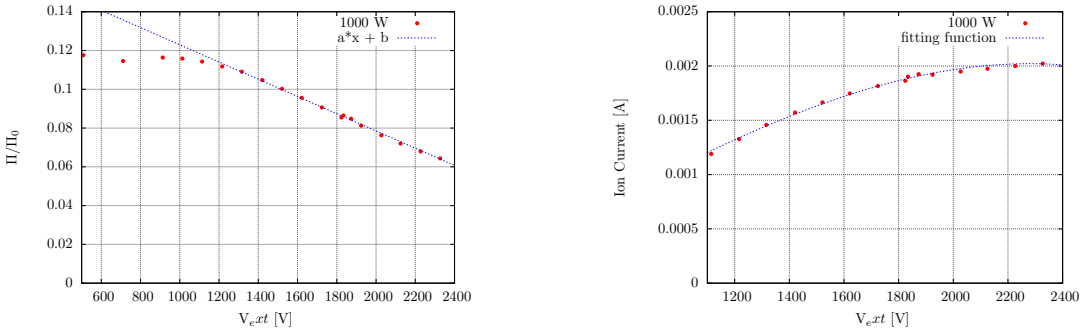


(a) (b)

Figure 3.11: 1000 W, 0.35 Pa source pressure, $V_{acc} = 15000$ V, Configuration II. In figure. In the left figure, $f(x) = a * x + b$, with $a = (-1.230 \pm 0.019)10^{-11}$ $A/V^{5/2}$ and $b = (4.659 \pm 0.032)10^{-8}$ $A/V^{3/2}$. In the right figure, $g(x) = -cV^{5/2} + dV^{3/2}$ , with $c = (1.220 \pm 0.020)10^{-11} A/V^{5/2}$ and $d = (4.639 \pm 0.041)10^{-8}$ $A/V^{3/2}$

Analyses of the PA and CFC current yield information about the beam optics which is linked to the beam divergence. Since it was not possible to use the Beam Emission Spectroscopy due to low extracted currents and the small Doppler shift of the emission line, the best optical conditions have been determined by electrical measurements on the PA and on the CFC. In fact, a wider beam will lose more ions on the post-acceleration grid with respect to a collimated one. For these reasons,

an estimation of the minimum of the beam divergence can be found following the ratio between the current gathered on the PA and CFC. Generally, the acceleration voltage is kept constant and the extraction voltage is changed until a minimum ratio is found.
In figure 3.9c a typical optics scan is reported. The ratio between PA and CFC tile currents was plotted against the ratio between the AG (fixed at 15 kV) and the EG : the lower this ratio, the better the beam optics. Due to the high complessity of beam physics, minima of the PA/CFC ratio generally need to be experimentally determined. Looking at 3.9c, preliminary consideration can be done: keeping the source pressure constant, the increase of the input radiofrequency power produces a left shift of the minimum, as reported in Table 3.5, therefore a proper optics calibration is needed for each different power input. This shift could be caused by modification of the electrostatic profile in the meniscus zone: in fact, if the input power increases, also the plasma ionization increases, thus producing higher density of charged particles that could induce this modification.
Since the data are not symmetric with respect to the minimum, a function with the form: $f(x) = ax^3 + bx^2 + cx + d$ was choosen and minima are reported in table 3.5

| Input Power | $V_{acc}/V_{ext}$ | *PA/CFC* |
|---|---|---|
| 500 W | $9.85 \pm 1.32$ | 0.4 |
| 700 W | $9.08 \pm 0.84$ | 0.375 |
| 900 W | $8.69 \pm 1.34$ | 0.375 |
| 1000 W | $8.67 \pm 1.36$ | 0.375 |

Table 3.5: Minima as a function of input power. The ratio between current is similar for each series, but it corresponds to lower AG/EG ratios. However the existence of plateaux has to be noticed; the higher the input power, the wider the plateau.

Previous scans were performed by keeping constant the source pressure, in order to evaluate also the contribution of the pressure change, some scans were collected at fixed power. An example can be observed in figures 3.12, where the extracted ion current increases as the pressure raises. These observations helps finding also better electron-ion ratio conditions: Considering results displayed in figures 3.5 and 3.14, figure 3.15a can be obtained; the higher the pressure, the lower the ratio.
Using data reported in figure 3.9c, a the current ratio was plotted as a function of the normalized perveance. The presence under-perveant and over-perveant zones can be easily seen.

It has been observed that the ratio between PA and CFC currents is influenced by source pressure: in figures 3.12 data taken at 900 W, 300 A filter, 10 V bias, 5 kV acceleration voltage and for different source pressures. Because of the existence of the EG voltage forbidden zone, only three pressures have been used to produce

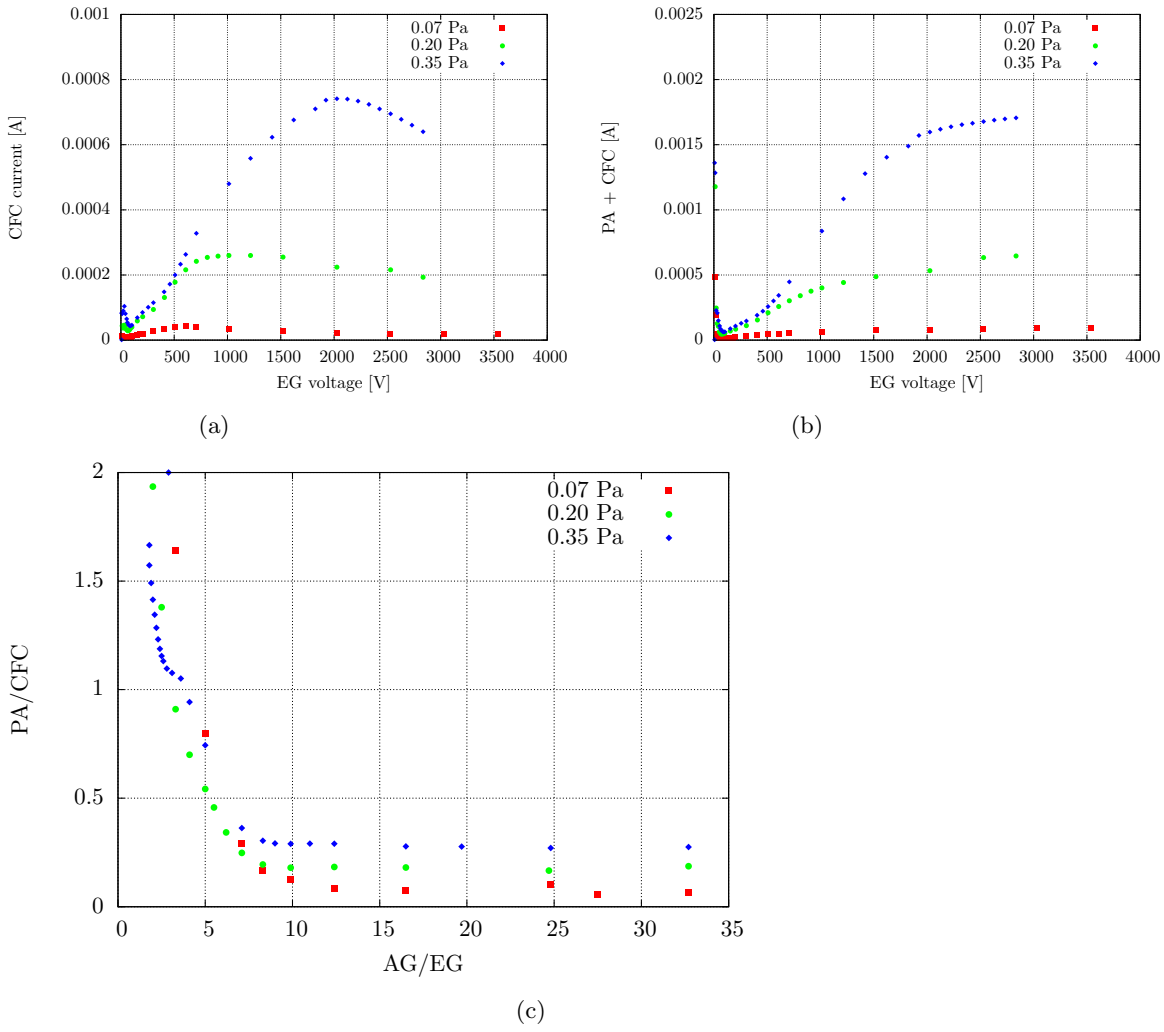


Figure 3.12: Pressure scan with fixed input RF power (900 W). Ion current increases by enhancing the source pressure. With these scans it was not possible to find a minimum. Probably due to pressure fluctations. 300 A filter, 10 V bias, 5 kV AG.

the plots. In these scans, the minimum PA/CFC currents ratio value can not be accurately determined, since the existence of plateaux. These plateaux extend from about AG/EG= 8 to AG/EG= 25 for all the three series; moreover, a during the scan at 0.35 Pa a problem occured with the gas valve since the overlap of two curves can be recognised, not allowing to complete the analysis. Nevertheless, some qualitative considerations can be made in order to characterize the extracted ion beam. The lower the pressure, the lower the extracted ion beam 3.14; remembering figure 3.5 it can be seen that the ratio between the electron current and the ion current decreases by enhancing the source pressure (figure 3.15a); moreover lower

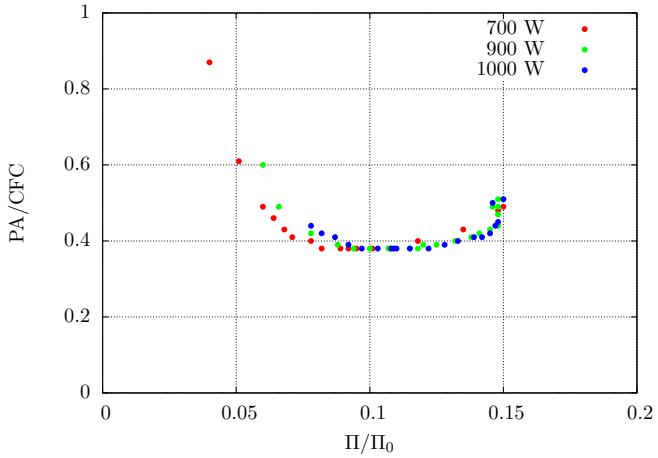


Figure 3.13: PA/CFC current ratio as a function of the normalized perveance, $\Pi/\Pi_0$, where $\Pi_0$ is the parameter found in equation 1.24 and $\Pi = I/V_{ext}^{3/2}$.

pressures yield a slightly lower PA/CFC ratio, as can be noticed in figure 3.12c.

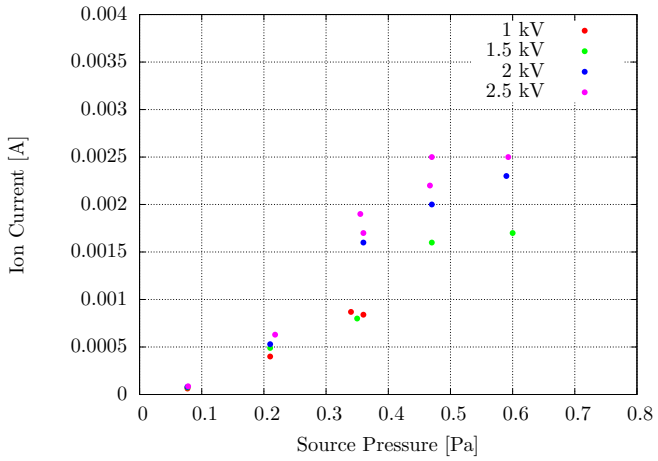


Figure 3.14: Ion current as a function of pressure. Data taken at 1000 W input power, 300 A in filter, 10 V Bias

Considering figure 3.15a, the currents can be written as $j_i = q\ n_i v_i$ and $j_i = q\ n_e v_e$ and their ratio is equal to:

$$\frac{j_e}{j_i} = \frac{n_e}{n_i}\sqrt{\frac{m_e}{m_i}} \tag{3.1}$$

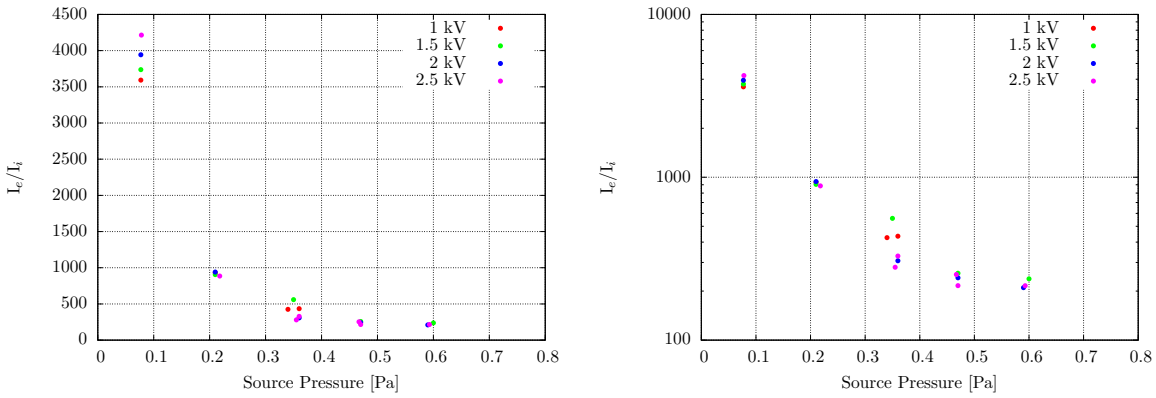


Figure 3.15: Electronic and ionic current ratio as a function of pressure. Data taken at 1000 W input power, 300 A in filter, 10 V Bias

where it has been hyphotized that particles have the same energy, since they are accelerated by the same grid. The ratio between current is known and it is possible to roughly estimate the ratio between densities. Considering 0.46 Pa, the ratio between currents is about 200 - 250: from equation 3.1, the ratio between $n_e$ and $n_i$ is about 1 and 1.5. The ratio estimation between densities is not precise, however it can be affirmed that ion density is comparable to the electronic density: both contribute to the meniscus electrical configuration.

Qualitatively, both pressure and radiofrequency power increase produce a more intense extracted beam. Best optics conditions are influenced by input power and pressure.

### 3.3.2 Acceleration voltage

The voltage difference between the grounded grid and the plasma grid is named acceleration voltage. This voltage determines the energy of the particles leaving the acceleration column. As reported in equation 1.25, the divergence depends also on the AG/EG ratio. It was found that if only AG voltage is increased a worsening of the optics conditions results. It is necessary to find the experimental condition that minimizes the divergence and then keep the $V_{acc}/V_{ext}$ constant. Experimentally, it was verified that working in this condition allows to preserve the minimum ratio between the current on the PA and the current on the CFC tile. An example is reported in Figure 3.16a, in which both total current (PA + CFC currents) and CFC tile currents are reported as functions of the voltages on the EG and the AG. Both currents present a monotone trend in contrast to that presented in Figure 3.9a, in which the ratio was not kept constant, thus resulting in a decrease of the CFC tile current after a threshold voltage value.

Both current in figure 3.16a presents a change of trend after a certain voltage (EG = 1500 V, AG = 12450 V for the figure shown), similarly to what is found in the EG voltage-current scans reported in figure 3.4a. Following the analysis performed on table 3.4, the first part of the total beam current was interpolated with the function $I = ax^{3/2}$. The fitting curve is shown in Figure 3.16b. Data displayed in figure 3.16a

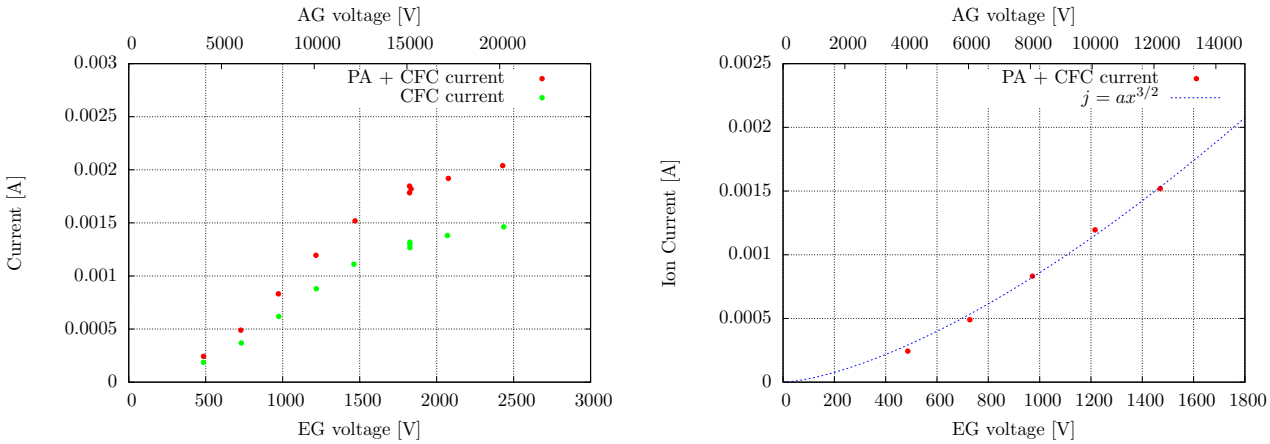


Figure 3.16: Fixed AG/EG ratio equal to 8.3. 1000 W , 300 A filter , 10 V bias , 0.35 Pa source pressure. In can be noticed that, keeping the ratio in the best optics condition, the CFC current does not present a decreasing trend. In the right figure it can be noticed how the Child-Langmuir Law is verified for the first points, as it was found for the electron currents. ($a = 2.717\ 10^{-8} \pm 0.049\ 10^{-8}$)

were taken using the AG/EG voltage ratio which minimized the PA/CFC with AG = 15 kV. However, as can be seen in table 3.6 where data corresponding to figure 3.16a are reported, the AG/EG ratio depends also on the absolute AG value.

| EG [V] | AG [V] | PA + CFC [mA] | PA/CFC |
|---|---|---|---|
| 486 | 4030 | 0.243 | 0.306 |
| 728 | 6070 | 0.489 | 0.325 |
| 972 | 8090 | 0.831 | 0.344 |
| 1216 | 12140 | 1.195 | 0.358 |
| 1470 | 10110 | 1.519 | 0.367 |
| 1834 | 15160 | 1.819 | 0.380 |
| 1824 | 15160 | 1.783 | 0.375 |
| 2076 | 17180 | 1.918 | 0.389 |
| 2429 | 20220 | 2.039 | 0.394 |

Table 3.6: Total beam current and PA/CFC ratio as a function of extraction and acceleration voltage. The ratio between voltages has been kept constant and equal to 8.3. It can be seen that the ratio between currents changes even if the best optical condition was used.

Data reported in table 3.6 evidences that also that at higher acceleration voltages, higher PA/CFC is found. In order to determine if the best optical condition depends not only on the ratio between voltages, but also on their absolute value, best optics scan have been performed at different constant AG and by varying the extraction voltage (figure3.17).

| AG [kV] | AG/EG | PA/CFC |
|---|---|---|
| 7 | $8.91 \pm 0.73$ | 0.303 |
| 10 | $8.04 \pm 0.91$ | 0.323 |
| 15 | $8.86 \pm 0.83$ | 0.345 |

Table 3.7: PA/CFC minimum as a function of the AG.
Position determined by a fitting function.

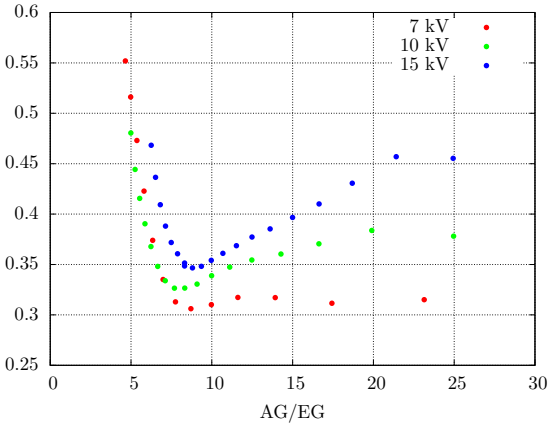


Figure 3.17: Minima as a function of the acceleration voltage. 800 W RF power, 20 Bias, 400 A filter current 0.35 Pa.

In figure 3.17 and table 3.7 it can be seen that the ratio between acceleration and extraction voltage for the minimum PA/CFC ratio current does not present a clear trend as a function of the AG voltage. The increase of the ratio could be caused by the space charge: the larger the extracted current, the more the reciprocal repulsion between ions, which could cause a greater beam divergence.
In order to provide a first evaluation of the contribution yielded by the acceleration voltage, the corrective factor $K$ was estimated by fitting the first part of the EG voltage - Ion current characteristic for scans obtained at 7, 10, 15 kV of acceleration voltage. The same function of figure 3.10 was used. This analysis provided preliminary information about how different extraction voltages affect the ion current. However, due to the lack of data, more scans with a larger range of acceleration voltages should be used in order to find how the ion current depends on the acceleration voltage.

### 3.3.3 Filter and Bias

The magnetic filter field contributes to avoid the negative ion destruction, as previously written. In figure 3.18a a filter field scan is reported, for different source bias voltages. It can be noticed that the magnetic field enhance yields a greater total ion current.

| AG [kV] | $a$ [$\times 10^{-8}$ A/V$^{3/2}$] | $K$ |
|---|---|---|
| 7 | $2.74 \pm 0.04$ | $0.123 \pm 0.001$ |
| 10 | $2.83 \pm 0.03$ | $0.129 \pm 0.001$ |
| 15 | $3.11 \pm 0.02$ | $0.139 \pm 0.001$ |

Table 3.8: Fit results using a function $I = aV^{3/2}$ on the first part of the EG voltage - Ion current characteristic for data taken at different acceleration voltages. 1000 RF input power, 0.35 Pa , 400 A filter field, 20 V source bias

Also the source bias polarization increases the total extracted current (figure 3.18b). These scans have been taken in the same operational conditions of those reported in figures 3.7a and 3.7b.

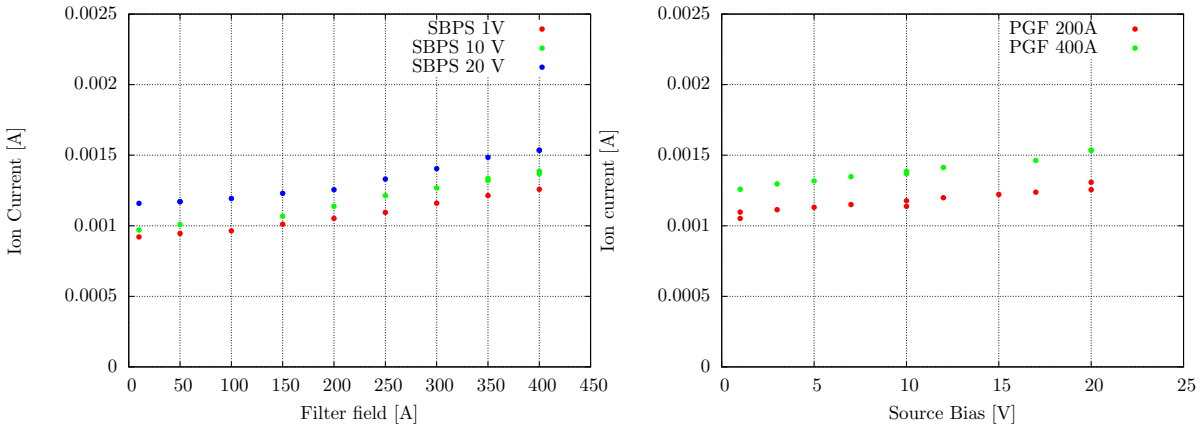


(a) (b)

Figure 3.18: 800 W input RF power, 0.35 Pa source pressure, EG voltage = 1500 V, AG voltage = 15000 V, Configuration II, PA/CFC $\approx 0.4$

Considering the filter field current scans (figure 3.7a and 3.18a), it can be concluded that no effect is present for currents lower than 100 A. Since these scans have been performed using the old magnetic configuration, in which the magnetic field was strongly localized between the plasma grid and the bias plate. As a consequence, at low filter currents the induced field is too weak to produce significant hot electron filtering. However, at higher currents (from 100 A to 400 A), a linear trend can be recognized both for ions and electrons.
Filter and bias yield a decrease of the ratio between the electronic current and the ion current. Even if a reduction of co-extracted electrons and an enhance of extracted ions can be obtained by acting on the filter and on the bias, it can be seen that this effect is quite low. For example, the ion current at the maximum filter

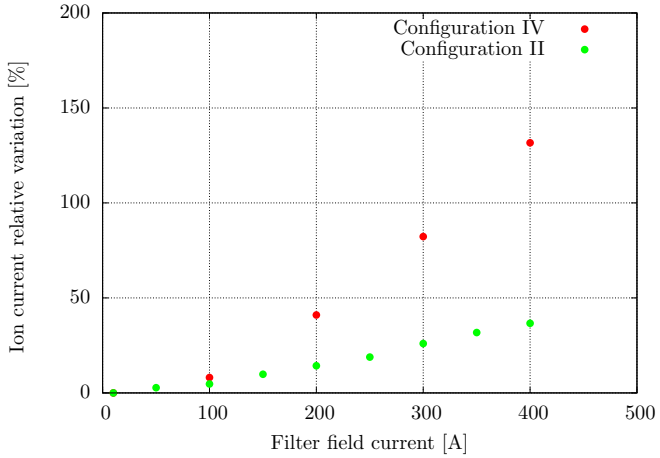


Figure 3.19: Comparison between the old magnetic circuit (in green) and the new magnetic circuit (in red). In y-axis the percentual variation with respect to the value at 10 A is reported.

current is higher only by 20% with respect to the case in which the filter off. These considerations led to the development of a new magnetic circuit; also the necessity of a larger bias interval for the PG emerged. (see the Appendix A).
The different effect of the new magnetic filter can be seen in figure 3.19, in which the two magnetic configurations are compared, considering the relative variation with respect to the lower value. In oxygen, the old magnetic circuit (green) yield a maximum increase of40 %, while the ion extraction enhancement produced by the new magnetic circuit is raised by 140 %.

## 3.4 IR thermocamera

Several consideration about beam optics were made in previous sections. However, to obtain a good estimation of beam divergence and beam uniformity, electrical measurements are not sufficient; for this purpose a infrared camera is used to record frames of the CFC tile rear side, since the BES was not able to provide information due to the low beam intensity.
If the beam were more intense, beamlet profile could have been visible. Results and analysis were performed in [22], however the main results are here discussed. In figures 3.20a and 3.20b, two frames of the rear side of the CFC tile are reported. Displayed images have been taken after 10s of heating, at $V_{acc} = 15$ kV; since the beam profile is a peak whose width is related to angular spread of beam particles, it is possible to measure the beam divergence from the thermocamera images and to find the experimental condition in which the divergence is minimised. The quantity used for characterize the peak width is the full width half maximum (FWHM). Both

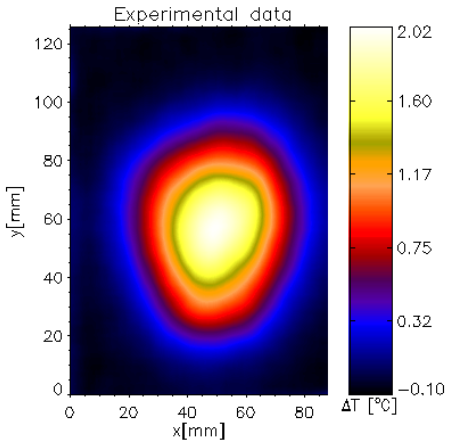


(a) $V_{ext}$ = 1.6 kV

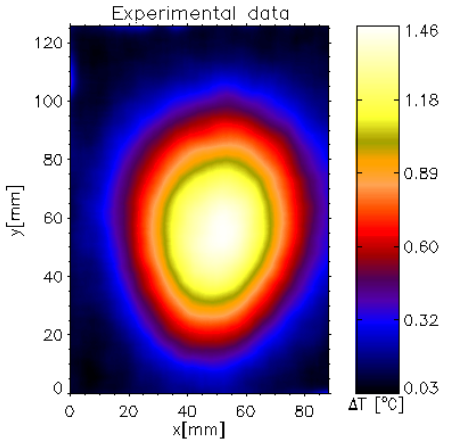


(b) $V_{ext}$ = 2.6 kV

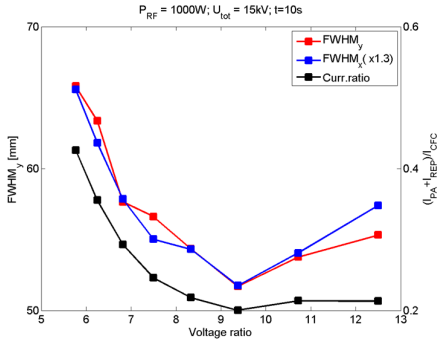


(c)

Figure 3.20: Comparison of the FWHMs with respect to data collected by electrical measurements.

FWHM along the x-axis and y-axis are measured and their ratio is about 1.3. The FWHM on the y direction is wider due to distorsion effects caused by magnetic fields placed in the accelerator. Thermographic analysis revealed that the $V_{acc}/V_{ext}$ value that minimize the FWHM is similar to the value found in figure 3.9c, as it can be seen in figure 3.20c, where data are reported.
However, the nine beamlets are not visible yet, due to the low beam current.

# Chapter 4

# Hydrogen operations

Hydrogen represents the most important gas for NIO1, since hydrogen and deuterium are the working gas in SPIDER and MITICA. Nowadays, hydrogen operations yield lower ion current with respect to oxygen. On the $24^{th}$ May 2016, a break in the pyrex insulator occurs. During the first operations after the shutdown, a fast spectroscopical analysis, showed many differences in source plasma behaviour, only partially due to the source cleaning.
To avoid further damages, hydrogen post-shutdown operations were performed with a maximum input power of 1000 W.
In this chapter, a short characterization of the reflected power provides preliminary information about source coupling. Then, an analysis on electron current and ion current is performed. The last section is devoted to compare the behaviour of the two gasses. A summary of the achieved ion current with hydrogen gas is reported in figure 4.1.

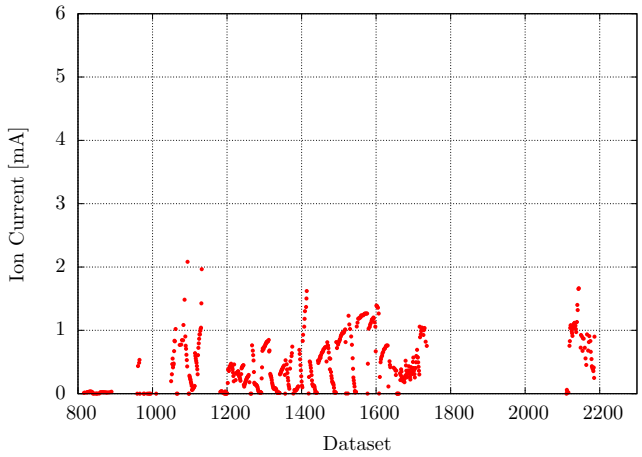


Figure 4.1: Summary of hydrogen operations. "Ion Current" is the current collected on the PA and on the CFC tile.

## 4.1 Reflected Power

Reflected power analysis provides first information about plasma behaviour. Many differences were observed between the inductive regime and the capacitive regime. The reflected power is mainly influenced by input power and source pressure. In

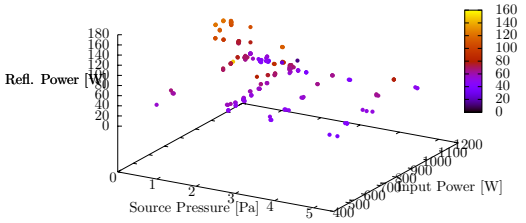


(a) Reflected power as a function of both source pressure and input power

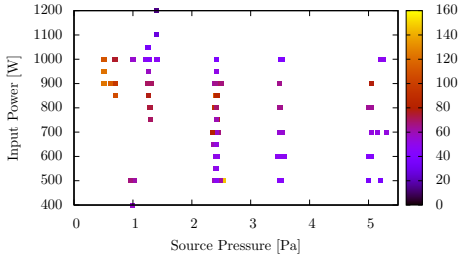


(b) Projection on x-y plane. In can be noticed by colour that when the transition to H-coupling happens, a reduction of the reflected power is obtained.

Figure 4.2: Reflected power during hydrogen operations

figures 4.2, the reflected power as a function of source pressure and input power is reported as a three-dimensional plot (splot-reflexed) and as a projection on the pressure-input power plane (splot-reflexed-map).
In figure 4.3b it can be noticed that the reflected power increases until 850 W are reached; at higher power, the reflected power decreases with a linear trend for all considered pressures. 900 W is the power in which the transition from capacive coupling to inductive coupling happens. If the pressure is increased over a threshold value of about 10 Pa, a return to the capacitive coupling was observed, with a significant increase of the reflected power.

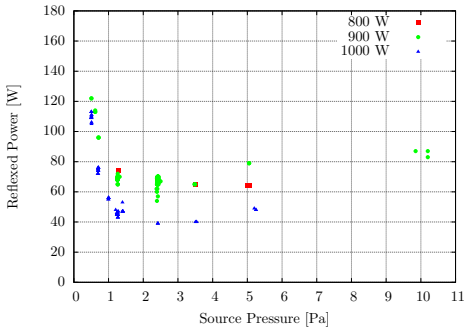


(a) Reflected power as a function of source pressure, for different input power series. 800 W series is referred to a capacitively coupled plasma.

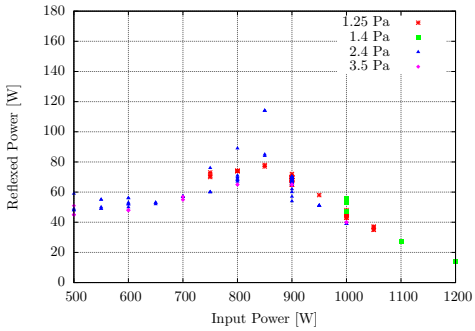


(b) Reflected power as a function of input power. Transition from capacitive regime and inductive regime happens between 850 W and 900 W. The reflected power changes trend after swithcing to the inductive coupling.

Figure 4.3

## 4.2 Electron Current

The current on the extraction grid is composed of electrons deflected by permanent magnets; being hydrogen lighter than oxygen, so stronger deviations of the beam on the extraction grid happen. Hydrogen negative ions can be absorbed on the extraction grid, as it has been found in simulations performed with OPERA software, and reported in figure 3.1.
Figure 4.4 reports the EG voltage-current scans obtained before May '16 shutdown.

Data between 0 and 400 V of extraction voltage are not available for this scan. Other scans have been performed after the shutdown and they will be treat later (figure 4.6a and 4.6b) However, displayed data trends are similar to those obtained in oxygen and the existence of a maximum is confirmed also for this gas, as displayed in figure 4.5.

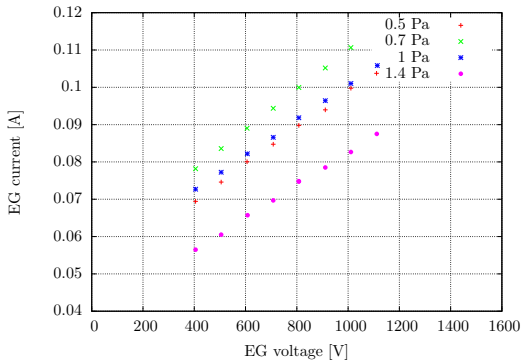


Figure 4.4: EG voltage-current characteriscs. Data taken at 1 kW of RF power, 300 A filter and 10 V bias.

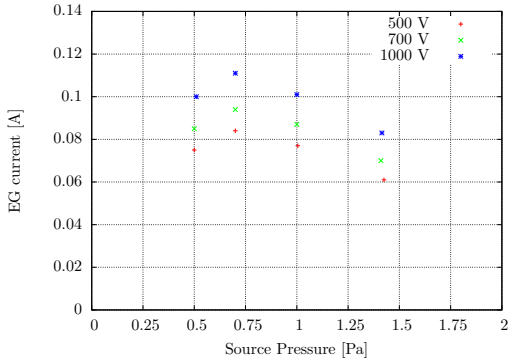


Figure 4.5: EG current as a function of the source pressure. A maximum exists in proximity of 0.7 Pa. Each series corresponds to a different EG voltage.

Data were fitted with the equation $ax + b$ and the trend of the fitting parameters is reported in table 4.1. The trend similarity near the saturation zone was also present in oxygen operation (Table3.2) providing a first confirmation of a similar dependence on EG voltages of the two gasses.

The full EG voltage-current scan, performed after the shutdown, shows a slight

| Source Pressure(Pa) | a ($\times 10^{-5}$ A/V) | b (A) |
|---|---|---|
| 0.5 | $4.86 \pm 0.07$ | $0.050 \pm 0.001$ |
| 0.7 | $5.35 \pm 0.02$ | $0.056 \pm 0.001$ |
| 1 | $4.69 \pm 0.03$ | $0.053566 \pm 0.00021$ |
| 1.4 | $4.38 \pm 0.06$ | $0.03881 \pm 0.00049$ |

Table 4.1: Linear fit of lines exposed in Figure 4.4

difference in the first part of the curve with respect to the oxygen (figure 4.6a and

4.6b): at voltages lower than 500, a different behaviour with respect to oxygen gas can be distinguished.

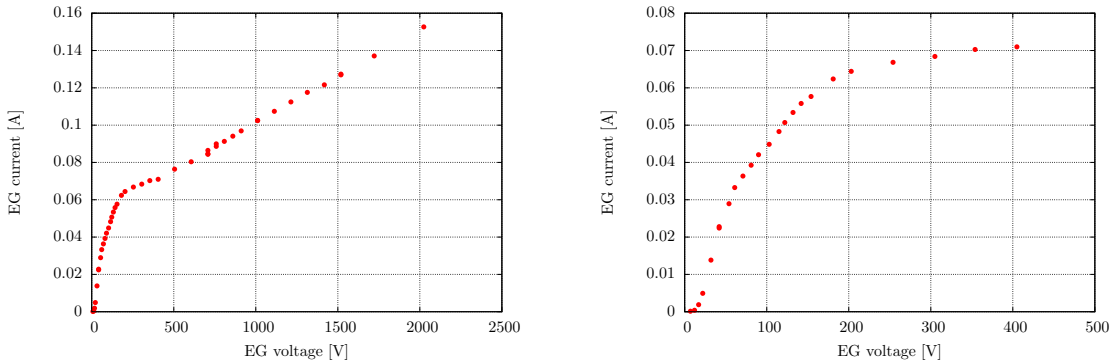


(a) (b)

Figure 4.6: In the left figure a complete EG voltage-current is reported. On the right a zoom in the first part of the curve is displayed. 1000 W input power 300A filter field current 10V source bias

Oxygen and hydrogen operations were performed using the same RF input power, while higher pressures were used in the latter. Different extracted electronic currents have been measured: for example, the electronic current extracted in hydrogen at 1000 V and 1000 W of input power (figure 4.6a) is comparable to the current extracted in oxygen at 1000 V and 500 W of input power. Moreover, oxygen switches to the inductive coupling at 400 W, while the power required to obtain an ICP in hydrogen operations is 850 W. It can be supposed that the these differences are mainly caused by the different ionization energy required by $H_2$ ($12.0697 \pm 0.0002$) and $O_2$ ($15.42593 \pm 0.00005$), according to [25]. The effect of the magnetic filter field and bias was tested also for this gas, finding that the main observation in oxygen are reproduced also for hydrogen operations.

These scans used the bias configuration II and in can be seen that the increase of the filter field or of bias voltage causes a reduction of the electron current on the EG ( 4.7). At the maximum filter field current the reduction of co-extracted electrons is about 20% with respect to a filter current of 100 A.

In order to evaluate the efficiency of the different configurations, data taken in configuration II have been compared to data in configuration V(figure 4.8), in which the new magnetic circuit was installed: it reduces the co-extracted electrons of 50 %: also in hydrogen operations the new magnetic circuit provide a greater reduction of the co-extracted electrons with respect to the old magnetic circuit.

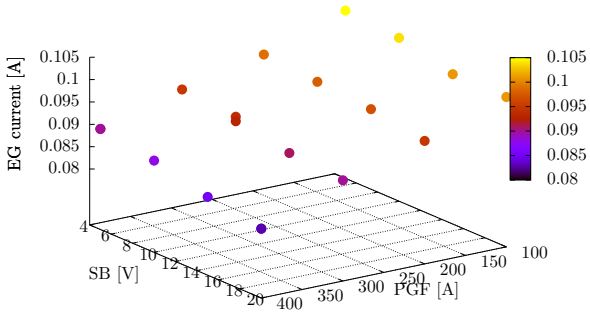


Figure 4.7: EG current as a function of magnetic filter and source bias polarization, Configuration II

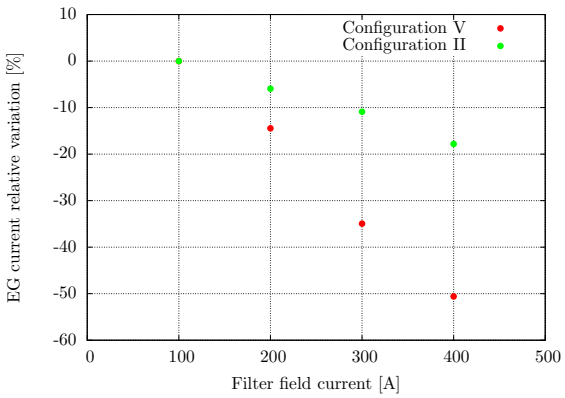


Figure 4.8: Comparison between the old magnetic circuit (in green) and the new magnetic circuit (in red). Currents have been normalized with respect to their maximum value.

## 4.3 Ion Current

Oxygen was used to test the acceleration system and the diagnostics, due to its higher ion production., but hydrogen operations are fundamental to increase NIO1 performances. Main scans and results will be exposed in this section; then, a comparison between hydrogen and oxygen will be performed.
Unlike oxygen operations, most of the extraction scans were performed at fixed input power (1000 W), in order to avoid source damages. These operations were generally performed at higher pressures with respect to oxygen gas, so a direct comparison is not possible.
Scan in EG voltage were collected in order to obtain a first characterization of hydrogen extraction beam. Measured beam and CFC current are reported in Figures 4.9a. Hydrogen extracted current reproduces the main feature of oxygen currents.

The extraction voltage influences the total negative ion current (Figure 4.9b ) which presents a non decreasing trend in the investigated range ( from 400 V to 1100 V). However, the current on the CFC tile presents a maximum current value; at higher EG voltage values, the optics worsens so much that the current on the tile decreases, even if the total beam current increases. It has to be noticed that the value of EG voltage which provides the maximum current on the CFC does not correspond to the EG voltage value that yields the best PA/CFC ratio.

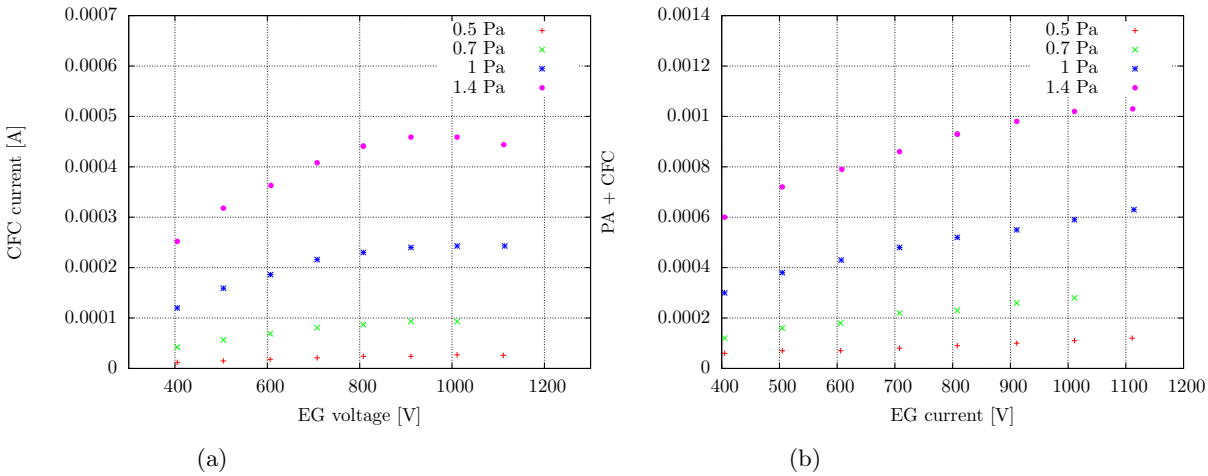


Figure 4.9: CFC current as a function of the EG for different source pressures (figure 4.9a) and CFC + PA current as a function of the EG for different source pressures (figure 4.9b). Data taken at 1000 W , 300 A filter , 10 V bias

The best optical condition was found in the same way as for oxygen operations, since the extracted beam is too weak to obtain a divergence value from BES diagnostic. As written before, since the beam divergence is linked to the ratio between the current collected on the PA and the current that impacts on the CFC tile, a first estimation of beam optics can be estimated.
In figure 4.10a the optics scans are reported. These scans were performed by keeping constant the acceleration voltage and by varying the extraction voltage, with 1000 W of RF power, 300 A filter and 10 V bias. Each coloured curve corresponds to a different source pressure. Minima are placed between AG/EG = 6 and 8, but the higher the source pressure, the flatter the scan curve. Because of instrumental errors, which are about the 1%, minima have been estimated using a suitable fitting function from AG/EG = 4 to AG/EG = 10.

Results obtained by the fitting function are reported in table 4.2. The high error is mainly caused by the few available data. More finely resolved scans could provide a characteristic curve with a lower uncertainty. For this reason it is not possible to

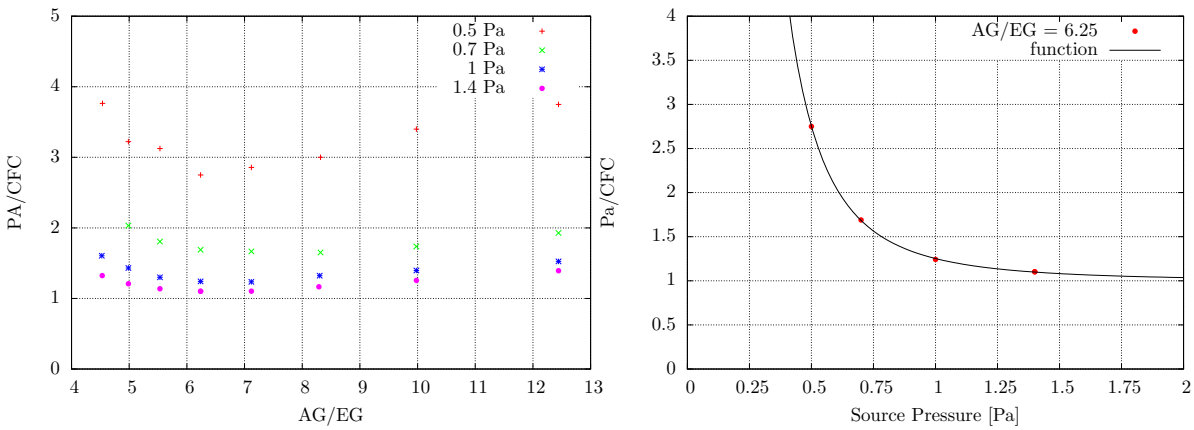


(a) (b)

Figure 4.10: In the left figure optics scans (ratio between the current on the PA and on the CFC tile) are reported for different pressures. It can be noticed that the minimum of each curve stands about at AG/EG = 6.25 or AG/EG = 7.10. In the right figure the minimum of each curve is reported as a function of source pressure.

| Pressure (Pa) | AG/EG minimum |
|---|---|
| 0.5 | $7.48 \pm 2.09$ |
| 0.7 | $7.99 \pm 2.25$ |
| 1 | $6.92 \pm 1.08$ |
| 1.4 | $6.82 \pm 1.01$ |

Table 4.2: Position of the minimum ratio between the PA current and the CFC current.

affirm if the minimum shifted by varying the pressure. However, a sort of plateau can be recognised, in which the ratio is constant, considering errors.
Since in the plateau points the ratio between the two currents is comparable, minimum ratio is plotted as a function of pressure In figure 4.10b; these values have been fitted with a power function, $f(x) = ax^{-b} + c$. This function is not intended to provide a universal trend of the ratio as a function of pressure, since more points should be required, but can provide a good approximation for this parameter in the investigated range of pressure.

Ratio between electronic and ionic density are reported in figures 4.11. Considering equation 3.1, it is possible to estimate the ratio between the electronic and ionic density.

| Parameter | Value |
|---|---|
| $a$ | $0.93 \pm 0.01$ |
| $b$ | $2.79 \pm 0.06$ |
| $c$ | $1.00 \pm 0.01$ |

Table 4.3: Power function parameters

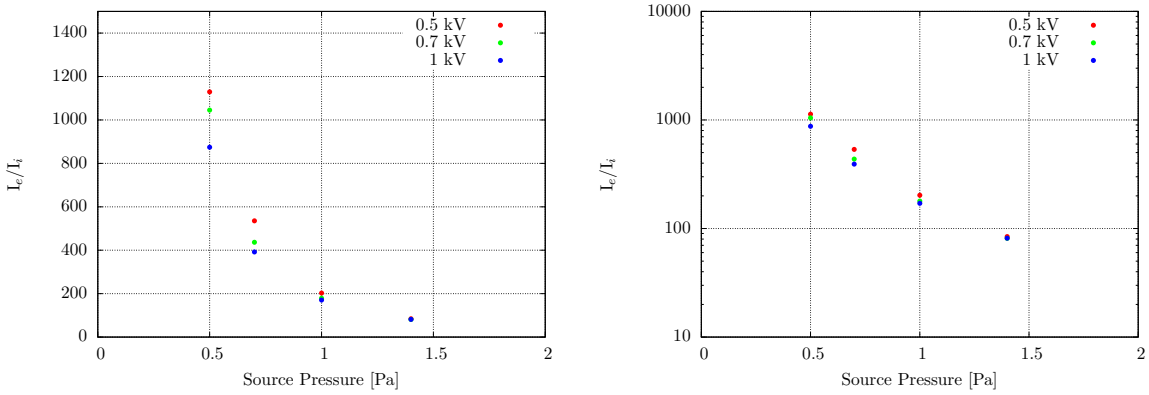


(a) (b)

Figure 4.11: Electronic and ionic current ratio as a function of pressure. Data taken at 1000 W input power, 300 A in filter, 10 V Bias, Configuration II

At 1.4 Pa, current ratio is between 80 and 90, therefore the ratio $n_e/n_i$ is about 1.8 - 2.1. Even if this estimation has a great error, the contribution of both species to the meniscus zone can not be neglected. In oxygen it was found (figure **??** that the minimum ratio between the two currents was about 200. Considering that they depends on the root of ion masses and condidering an equal electronic density, the ratio between $j_{0\_}$ and $j_{H\_}$ should be equal to 4. If the densities of the two ion species are compared, the ratio is about 3, lower than the expected one. This could be caused by the fact that in hydrogen (figure 4.11) a saturation level of the ratio between currents against the source pressure was not reached yet. Further studies are necessary in order to reduce the electronic density and to evaluate its effect on the meniscus.

Raising the source pressure not only increases the total extracted ions, but also it lowers the ratio between the current lost on the PA and the current that impact on the CFC tile. However, the higher the pressure, the more frequent the breakdowns between grids. Breakdowns prevented from reaching higher performances in extraction and acceleration, thus reducing total ion current. Ion current is also limited by the lower hydrogen electronegativity with respect to oxygen, with a further reduction of the extract total current. Since it was difficult to reach 10 kV in

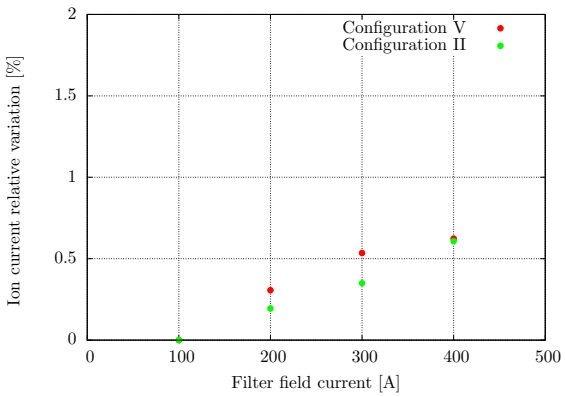


Figure 4.12: Comparison between the old magnetic circuit (in green) and the new magnetic circuit (in red). Currents have been normalized with respect to their maximum value.

acceleration voltage, it is not possible to provide an acceleration voltage analysis. In the previous section it was speculated about a different ionization degree between oxygen and hydrogen at 1000 W: more confirmations are required in order to verify this hypothesis; however, if it were verified, a further explanation to the different extracted current would be provided.

### 4.3.1 Comparison between H and O ion current

The ion current in hydrogen is very lower with respect to the current foreseen in NIO1 when the maximum RF power, extraction voltage and acceleration voltage will be reached. Moreover, the caesium oven has not been implemented yet; so the ions are produced only by volume production. After the caesium oven installation, the ion surface production will enhance the negative ion density up to a factor of 10.

With respect to oxygen operations lower beam currents were produced at the same radiofrequency input power, even if higher source pressure was used. This can be explained with some considerations:

- Hydrogen and Oxygen have different electronegativity: the first has a value equal to 2.2, while the oxygen electronegativity is equal to 3.44. For this reason, it can be supposed that the ion destruction cross section due to hot electrons is lower in oxygen than in hydrogen; thus a greater portion of ion is created and, then, extracted.

- Hydrogen is about 16 times lighter than oxygen. Because of the dependence of the mass in the Larmor radius, it can be expected that hydrogen ions between the PG and the EG receive a larger deviation with respect to oxygen ions, leading them onto the EG where they are lost

Since the Larmor radius is given by:

$$R_L = \frac{mv_\perp}{eB}$$

it can be increased by raising the velocity of the ions perpendicular to the magnetic fields. This should be achieved by enhancing acceleration voltage.

- Hydrogen transition from capacitive regime to inductive regime happens about at 850-900 W of input power. Since extraction operations were performed at 900 W or 1000 W, it can be supposed that, at this powers, a full inductive mode has not been achieved yet and only a small amount of negative ions is produced.

The trend of the extracted beam current as a function of the EG voltage was discussed in chapter 3. It was established the indipendence of the ion current in the first part of the curve from the input power. Normally the input power has the effect of increasing the voltage range in which the Child-Langmuir Law exists, while an acceleration voltage increase produces a total beam current raise. In the further analysis the maximum voltage in which the law can be applied, will be named *maximum voltage* or $V_{max}$ . It is possible to compare the two different gas data also at different input power; providing to keep the AG voltage constant, power and pressure difference provide a shift of the maximum voltage.

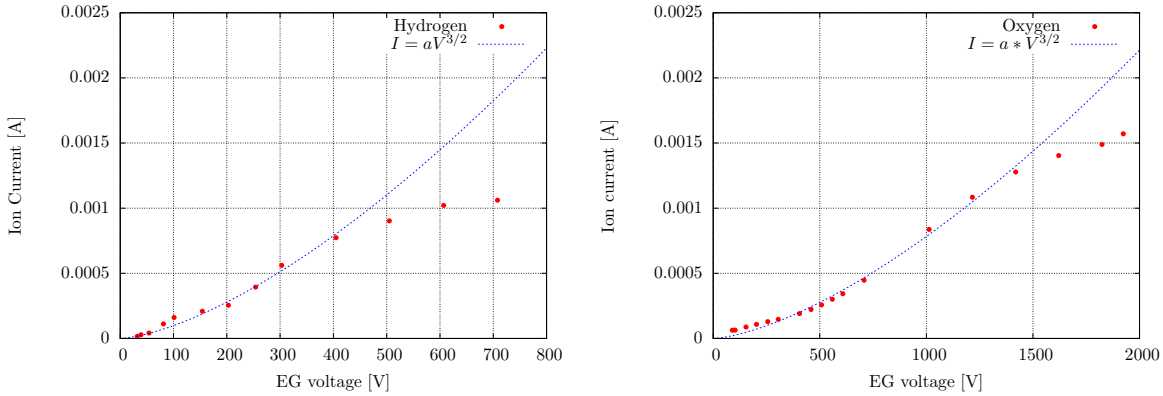


(a) (b)

Figure 4.13: Comparison of the trend described by the Child-Langmuir law between hydrogen and oxygen.

In Figures 4.13 the first part of the voltage-ion characteristic is shown for hydrogen and oxygen. The acceleration voltage is 5 kV. Since the Child-Langmuir law is influenced by gas properties only through the root square of the mass, it is expected that,:

$$\frac{\Pi_{O_2}^{teor}}{\Pi_{H_2}^{teor}} = \sqrt{\frac{m_H}{m_O}} = 3.984 \tag{4.1}$$

The results of the fit are reported in table 4.4:

| Gas | $a^{fit}$ ($\times 10^{-8}$ A/V$^{3/2}$) |
|---|---|
| $0_2$ | $2.475 \pm 0.07$ |
| $H_2$ | $9.852 \pm 0.29$ |

Table 4.4

The experimental ratio $\frac{a^{fit}_{O_2}}{a^{fit}_{H_2}} = 3.980 \pm 0.010$ is compatible equation 4.1. It can be concluded that hydrogen and oxygen are extracted and accelerated in the same ways. Earlier, to explain the low hydrogen extracted current, it was speculated about a hydrogen collection by the EG. However, this result proves that this is not the case. Another possible explanation considers the maximum EG voltage reached by the two different gasses; for hydrogen at 1000 W it is of 400 V, against the 1400 V reached by oxygen. This means that hydrogen beams enter the saturation range at lower voltages than oxygen not allowing to obtain higher currents. In order to increase the hydrogen ion current one way is to to reach higher input radiofrequency powers, thus producing an increasing of the maximum achievable voltage.

## 4.4 Bias System

The configuration V [31] was installed at the end of July: In this configuration, the negative pole of the power supply is connected to the $BP_e$, while the positive pole is connected to the PG; $BP_e$ and $BP_m$ are connected to each other.
Some scans were performed by keeping the PG filter current current and the source bias constant. During these scans it was not observed a monotonic decrease of electrons on the EG nor a monotonic increase for ions. By polarizing the bias plate with respect to the plasma grid it is possible to attract electrons in order to decrease the electronic density in the meniscus zone, thus increasing the ion extraction. The maximum efficiency was reached for a voltage equal to 10 V. Very few data have been taken using this configuration: a proper characterization will be performed during future operations.

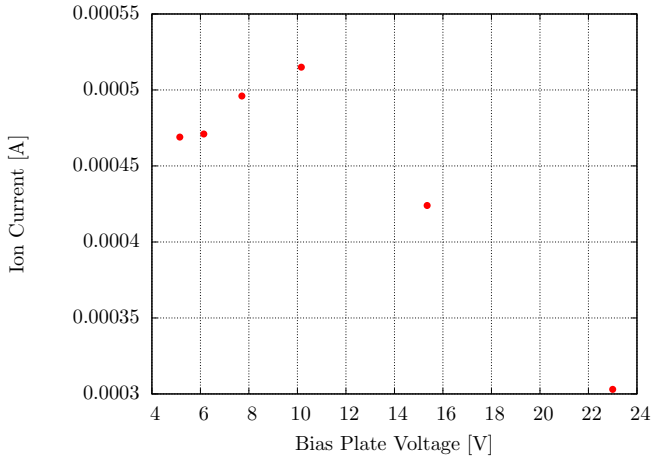


Figure 4.14: Effect of the polarization of the bias plate with respect to the PG. It can be noticed that the maximum efficiency in ion productions is produced at about 10V

## 4.5 IR thermocamera

Thermocamera images were collected also during hydrogen operations, even if the beam intensity is weaker with respect to oxygen. The complete analysis can be found here [22]; in this section the main results will be exposed, comparing them with oxygen operations. Frames were collected during an optics scan, by keeping

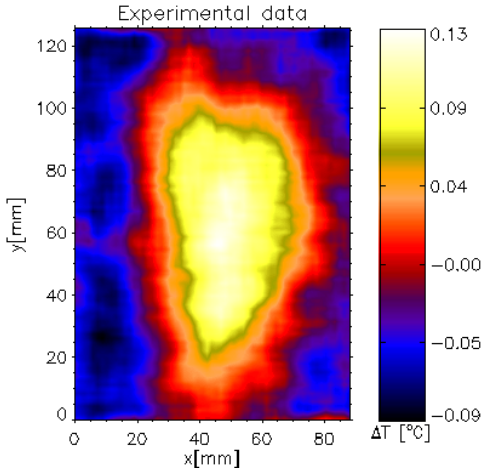


(a) $V_{ext}$ = kV

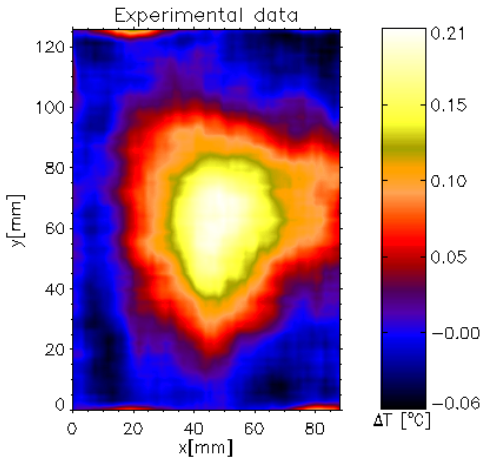


(b) $V_{ext}$ = kV

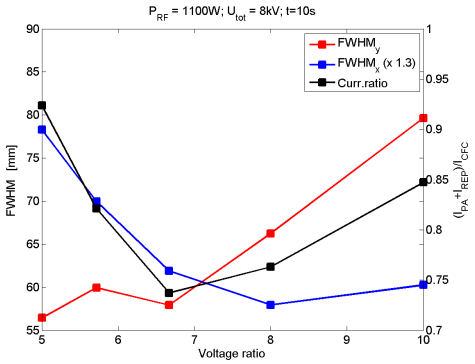


(c) $V_{ext}$ = kV

Figure 4.15: Comparison of the FWHMs with respect to data collected by electrical measurements.

fixed the $V_{acc}$ and by varying the $V_{ext}$.Frames are less clear with respect to oxygen ones, due to the lower intensity of the beam. For this reason, only x-FWHM yields results in accordance to those obtained by electrical data.

# Chapter 5

# Electronic density estimations

The electronic density is a fundamental parameter which can be linked to the ionization degree and it can be used to obtain several important parameters, such as the plasma frequency $\omega_p$, the skin depth $\delta$, plasma conductivity $\sigma_{el}$ and collision frequencies. Generally, it is possible to obtain it by using Langmuir probes or by using spectroscopic techniques, that will be discussed in chapter 5.1. Due to the lack of probes, an alternative method is proposed: it is based on the same principles of the Langmuir probe.

## 5.1 Spectroscopy

To monitor the source by analysing the emitted electromagnetic radiation in NIO1, Optical Emission Spectroscopy is used. Collected data are elaborated using spectral lines in order to determine several plasma parameters.
The results presented in this chapter have been obtained using a mixture of oxygen (90%) and argon (10%), Since no suitable method was found to analyze a pure oxygen spectrum, argon was introduced and its spectra analyzed using ADAS software package.[26] [27]
Photons are collected along two lines of sights by optics heads, equipped with plano-convex BK7 lenses of 50 mm focal lenght and 4 mm clear aperture [26].
Collected signals are then transmitted on silica-silica optical fibers with 400 $\mu$m core diameter. One of the two fibers is connected to a low resolution spectrometer (*Hamamatsu C10082CAH*), [28] that mounts an integrated back thinned CCD sensor of 2048 pixels. It can record spectra between 350 and 850 $nm$, with 1 nm resolution. This spectrometer is generally used for a qualitative survey of the plasma source, in order to detect the presence of impurities in the plasma. The second fiber was connected to high resolution spectrometer (*Acton SpectraPro-750*) [29], equipped with a 2D back illuminated frame transfer CCD camera of $512 \times 512$, for 6 nm wide spectral window and a resolution of 50 pm. This spectrometer was used to measure the intensity of argon lines from which the electron temperature and

density were obtained. The LOS of the two instruments are parallel to the PG, at a distance of 19 mm (figure 5.1)
The electronic temperature and density can be obtained by considering the ratio between the intensity of the $Ar^+$ lines at 480.6nm and 488.0nm and the Ar line at 750.40nm and by using aiterative process [26]

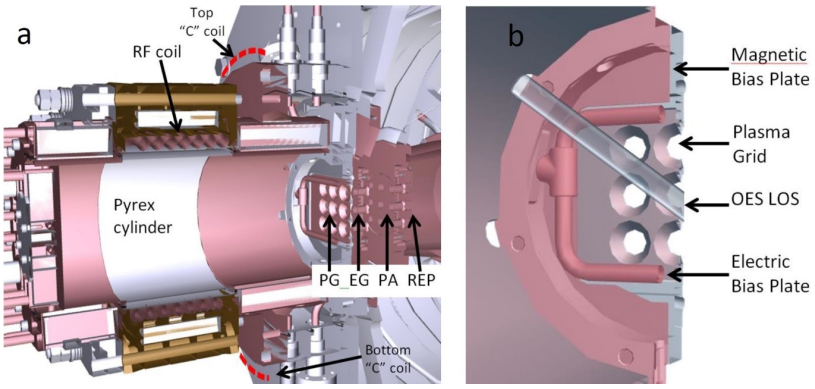


Figure 5.1: Source sketch. In the right figure it is possible to the OES LOS.

Emission spectra were collected using configuration IV, at 0.48 Pa, in which the filter current flows through the PG and the C-coils; the two bias plate components were connected to each other and left at floating potential. In this filter configuration, the magnetic field in the LOS zone is about 7.5 G per 100A filter current. RF power, source bias and the magnetic filter current were changed in order to evaluate their effect on electronic temperature and density. Results as a functions of RF power and filter current are reported in figures 5.2.
According to a simplified model [30], regarding the balance between ions produced

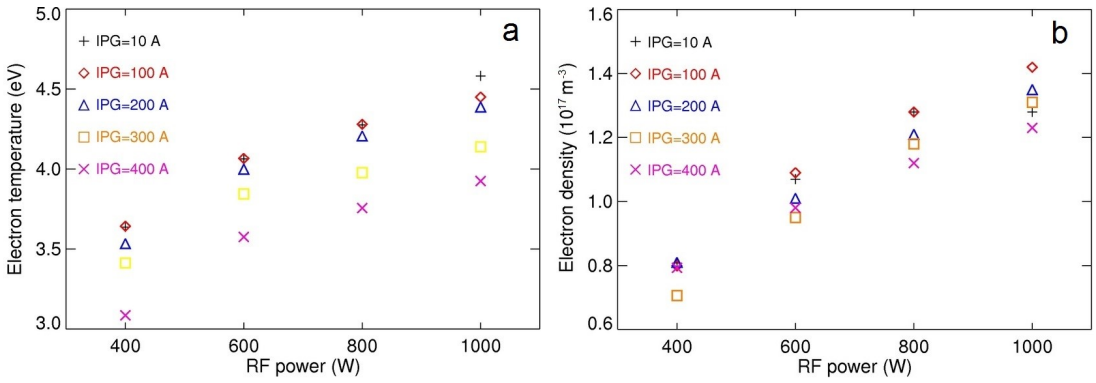


Figure 5.2: Electron temperature (left) and density (right) as a function of the input RF power. Error about 10%

by collisions with electrons and ions lost on the source walls, it is expected that

electronic temperature does not depend on electronic density. Moreover, higher RF power yields an increase in electronic density, but electronic temperature is not affected by this enhancement. This theory is not fully confirmed. In fact, as it can be seen from the experimental data reported in figure 5.2, while $n_e$ increases with higher injected power as expected from the theoretical model, also the electronic temperature increases. In the same figure, also the effect of the filter is visible. In fact, by increasing the filter current, lower electronic density and temperature are detected near the plasma grid. The density decrease between a filter field current of at 100 A and 400 A is in the order of the 10% - 15%, well within the level of systematic errors.
Spectroscopy allows to determine the trend of the electronic temperature as a function of the source pressure and the effect of the source bias in the reduction of the electronic density in the meniscus zone (figure 5.3). In the graph on the left it is possible to see how the dependence of the electronic temperature by source pressure, as expected in [33]. Moreover, it can be noticed that the new magnetic configuration (white) is more efficient with respect to the old magnetic configuration (red).
In the right graph, the electronic density near the PG as a function of the bias is shown.

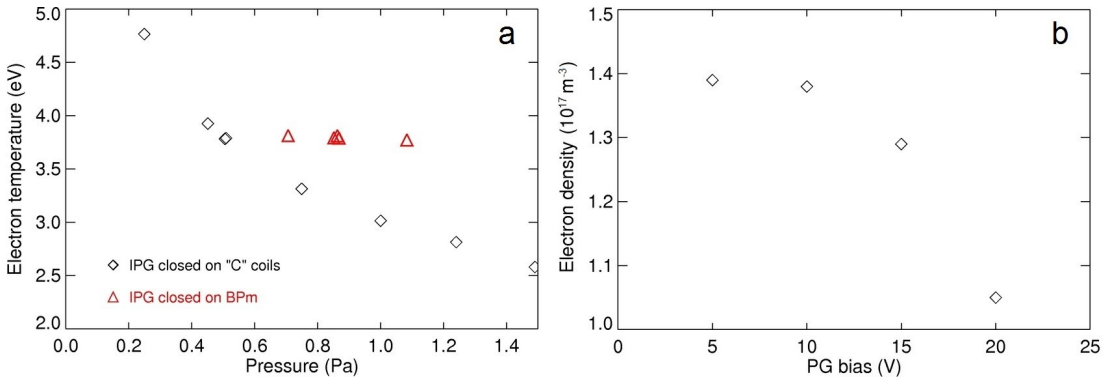


Figure 5.3: Figure a): electronic temperature as a function of the pressure. Data corresponding to the new magnetic circuit are in white, while those referred to the old magnetic circuit are in red. Figure b): Electronic density as a function of the source bias. Error are about the 10%.

## 5.2 Electrical data

The Langmuir probe [32] consists of an electrode inserted in the plasma. By polarizing the probe with respect to a reference electrode, generally the vacuum vessel, the characteristic curve reported in figure 5.4 can be obtained.

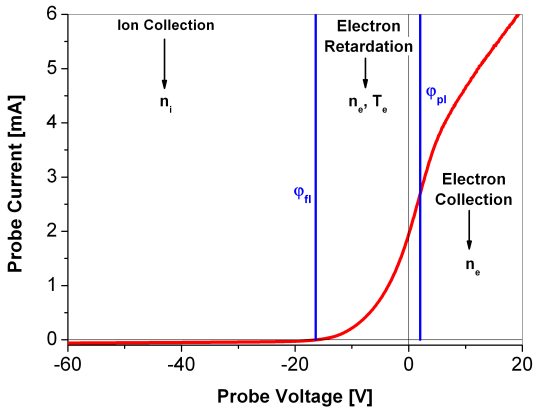


Figure 5.4: Langmuir probe characteristic curve.

In the figure the existence of three intervals can be noticed. The left limit yields the ionic saturation current, while the electronic saturation current is shown on the right-hand side. These two portions are connected by an exponential function. The potential for which the curve deviates from the exponential trend current is named *Plasma Potential*, while the potential for which the collected current is zero is referred to as *Floating Potential*. The ionic saturation current can be written as:

$$I_{is} = \frac{1}{2} e A n_0 c_s \tag{5.1}$$

where A is the probe surface, $n_0$ is the density and $c_s = \sqrt{T_e/m_i}$ the ion sound speed. The electronic saturation current can be expressed as:

$$I_{es} = \frac{1}{4} e A n_0 v_{te} \tag{5.2}$$

where $v_{te} = \sqrt{8T/\pi m_e}$ is the thermal electronic speed. Since the plasma is globally neutral, $n_0 = n_i = n_e$. From the electronic saturation current, the density of negative particles can be obtained:

$$n_0 = \frac{I_{se}\sqrt{2\pi m_e}}{eA\sqrt{T_e}} \tag{5.3}$$

Since the electrons react faster to the potential variation due to their lower mass with respect to ion mass, it can be affirmed that the collected current is formed

mainly by electrons. This first method used the plasma grid as the electrode of the Langmuir probe. By varying the polarization, a V-I characteristic curve, similar to figure 5.4, was obtained. Using a logarithmic scale, a change of trend can be recognised and the corresponding voltage can be identified as the plasma potential: at this value, the current collected on the PG for this voltage can be considered the electronic saturation current. In figure 5.5 an example of the V-I characteristic curve obtained by polarizing the plasma grid by means of the the SBPS is reported.

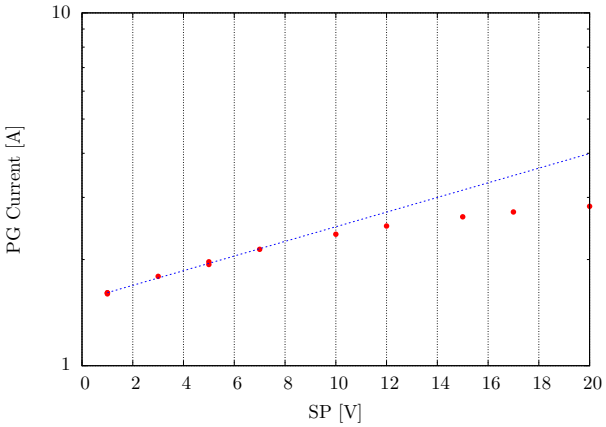


Figure 5.5: Example of the V-I characteristic, obtained considering the bias and the current on the PG. The plasma potential correspond to the voltage in which the characteristic ends its exponential trend (blue line).

By equation 5.3, it is possible to obtain an estimation of the electronic density. However, this equation yields electronic densities lower of a factor 10 with respect to spectroscopical data. In fact, this equation can be used if the plasma can be considered infinite and if it can provide infinite charged particles, but this hypothesis is not verified in NIO1 source. The plasma grid has to be considered as the anode of a double asymmetric Langmuir probe since the area of the PG and the area of the walls are not comparable and electronic density can be estimated using equation 5.1 instead of equation 5.3.
In fact, a positive ion current is attracted to the source wall, in order to compensate the negative current on the PG, therefore $I^+ = I_{is} = I_{es}$. A surface estimation, based on NIO1 project, was performed and the area on which positive ions are accelerated is A = 0.045 $m^2$. Electronic temperature can be choose in a range between 2 and 4 eV, as expected from simulations and confirmed by spectroscopical analyses; this variation does not introduce a great error, since in the former formula the square of the temperature appears. The density can be written as:

$$n_0 = \frac{2I}{eA}\sqrt{\frac{m_i}{T_e}} \tag{5.4}$$

Considering this langmuir probe configuration, density results have the same order of magnitude as spectroscopy measurements, as can be seen in figure 5.6b.

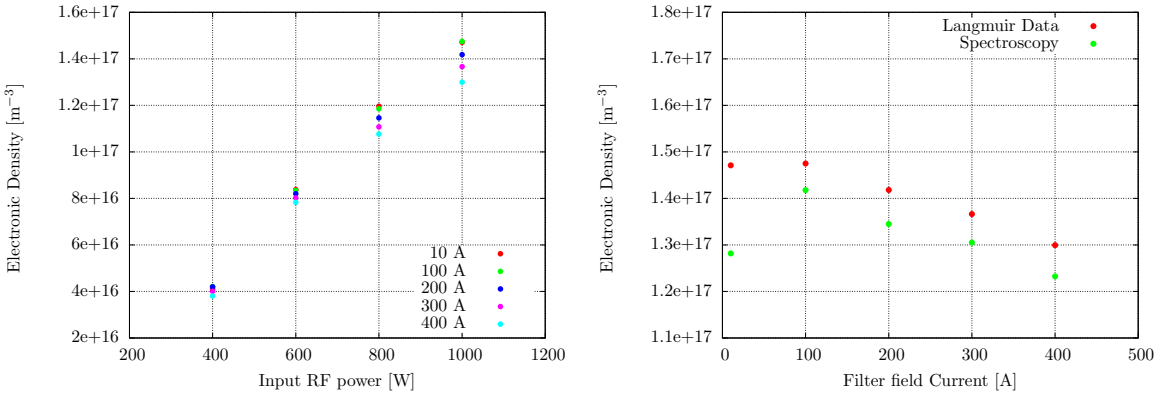


(a) (b)

Figure 5.6: Electronic density estimations using double asymmetric langmuir probe principles. In the left figure, $n_e$ as a function of the input power is displayed. Each series corresponds to a different filter current value. In the right figure a comparison between values of $n_e$ obtained by spectroscopy (red) and electrical measurements (green) is shown. It can be seen that values are comparable within the errors, that are about $10 - 20\%$.

A comparison between electronic densities in hydrogen and oxygen (using the same RF input power) is proposed in figure 5.7a.

It can be seen that, using the same input power, electronic density in hydrogen

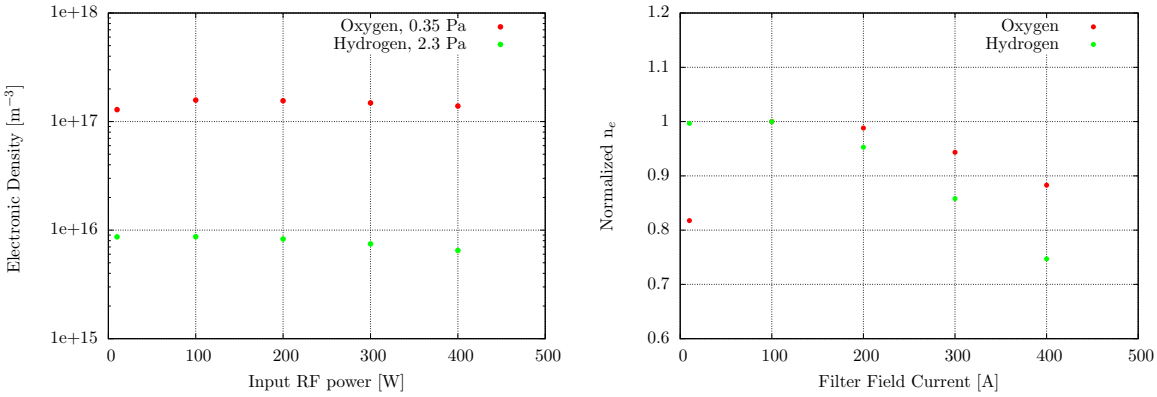


(a) (b)

Figure 5.7: 5.7a): Estimated electronic density by using the langmuir probe model. Densities otained by equation 5.3. 5.7b): Densities normalized to their value at 100 A. It can be noticed the higher effect of the magnetic field on hydrogen electronic density

operations is lower by an order of magnitude with respect to oxygen. It was proposed in former chapters that lower hydrogen extraction performances were caused by a lower ionization degree: data exposed in figure provide a further proof for this hypothesis. In figure 5.7b, electronic density normalized values are compared and it has found that using hydrogen $n_e$ is reduced of 25 % at 400 A, while in oxygen $n_e$ is reduced only of 12 %.

# Chapter 6

# Conclusions

In the framework of the research for ITER experiment, the development of external heating systems is fundamental. The neutral beam injector prototype, that will operate at Consorzio RFX requires preliminary studies, in order to validate numerical codes and test diagnostic systems. For this purpose, a smaller and more flexible negative ion source was developed.
During this thesis activity a first NIO1 beam characterization was performed. Former works were focused on the source characterization, while in this work the main analysis was focused on the extracted beam. Due to the relative low input power, the absence of caesium oven and the accelerator not used at its maximum capability, the extracted beam has an intensit too low for being properly diagnosed. The beam intensity was too weak to allow a reliable BES analysis and alos thermographic analyses performed using a CFC tile could be only partially used. The beam analysis could rely only on eletrical measurements. The accelerator was tested using oxygen gas: due to its higher electronegativity it is possible to obtain higher negative ion density with respect to hydrogen. During oxygen operations both the electronic current, absorbed on the extraction grid and the total ion current were analyzed, in order to provide a preliminary characterization of beam properties. Since for further operations the reduction of co-extracted electrons is fundamental, first analyses were devoted to find operational conditions that minimize the electronic current collected on the extraction grid, by changing input RF power or source pressure. The effect of the magnetic filter field and the source bias were analyzed, demonstrating that they yield a reduction of co-extracted electron current.
Ion current, composed by ions collected on the PA and on the CFC tile, was studied as a function of source pressure and input radiofrequency power. In the lack of divergence measurements it has been proved that the ratio of the current on PA and CFC could be used instead. The condition of less divergent extracted beam corresponds to a lower current reaching the PA. It was observed that the ratio between the acceleration voltage and extraction voltage which minimize the PA/CFC current ratio depends on RF input power. This dependence should be better studied during

future operations at higher RF input power.
As expected, it was confirmed that operating using the $V_{acc}/V_{ext}$ constant improves the current on the CFC tile, since in this condition the beam divergence is minimized.
Ion current characteristic has been studied: it was observed that the Child-Langmuir law holds only for low extraction voltages, whereas at higher $V_{ext}$ ion depletion occurs in the meniscus zone. The increase of the acceleration voltage causes an increment of the total ion current: however, since scans were mainly focused on extraction voltage, a complete analysis was not completed.
The effect of the magnetic filter field was considered, observing that higher filter field allows to extract higher ion current. Biasing the source with respect to the wall ion increase is observed. A mixture of oxygen and argon was used to obtain information about the electronic temperature and density near the plasma grid, using the Optical Emission Spectroscopy. This diagnostic confirms some results expected by simulations, such as the increment of the electronic density with the RF power and the decrease of the electronic temperature with the increase of the source pressure.
After extraction test with oxygen gas, hydrogen operations were performed. Hydrogen negative ion beam is weaker with respect to the oxygen beam, mainly because of its lower electronegativity. When operated in hydrogen NIO1 plasma switches to inductive coupling at about 850 - 900 W: since operations were performed at a maximum power of 1000 W it was also supposed that a full transition to the inductive regime was not achieved, thus lowering the coupling efficiency and producing a lower ion density. Hydrogen operations were devoted to reproduce main trends obtained during oxygen operations; some difference were found in the EG voltage-current characteristic curves, however due to the lack of data this difference should be better analyzed during next operations.
A comparison between the hydrogen and oxygen extracted currents revealed that hydrogen beam is weaker mainly because of the low ion density and not caused by other effects, such as the beam deviation produced by EG magnets. Several electric configurations were tested and two different magnetic filter field circuits were employed. The new circuit is placed at 60 mm from the PG and generated a more delocalized magnetic filter field. Since the filter effect is proportional to its spatial width, this new circuit is more efficient to prevent high energy electrons from diffusing from the driver to the extraction zone and it was verified that higher ion currents were extracted. In the latest experimental days, the two components of the bias plate biased by to a power supply, in order to reduce the electronic density in the extraction zone: this last configuration will be further studied in the future.
Using the current collected on the PG by biasing it with respect to the source body, a double asymmetric Langmuir probe-like density estimation was obtained; this result was compared with that obtained using the OES. Both trends and absolute values are compatible with those estimated using the Optical Emission Spectroscopy. Because of the good accordance between values obtained with these two different

methods, an estimation of the electronic density in hydrogen was performed: this estimation yields a density lower by an order of magnitude with respect to oxygen; considering that in hydrogen the operating pressure is higher than in oxygen, this difference indicates a smaller degree of ionization which can explain the lower extraction performances obtained during hydrogen operations.
The ratio between ionic and electronic currents was considered for both species and it was found that in the extraction zone the density of ions is similar to the density of electrons: a reduction is necessary to achieve higher ion current. This characterization were mainly performed using electrical measurements. When extracted ion beams will reach higher intensity such that they can be analyzed by thermocamera, static calorimeter and beam emission spectroscopy, a more complete characterization will be possible.

# Appendices

# Appendix A

# Bias Plate and Filter configuration

During NIO1 operations, several electric and magnetic configurations were tested in order to reduce the amount of co-extracted electrons and to improve the negative ion extraction.
Two magnetic circuits were used (figure A.1):

- *Old Magnetic Configuration*: The magnetic field is created by current flowing through the PG and returning to the power supply through the $BP_m$, placed at 6.8mm from the PG.

- *New Magnetic Configuration*: The magnetic filter field is produced by current flowing through the PG and returning to the power supply through the C-shaped circuit, placed at 60 mm from the source.

The expected magnetic field for those configurations can be seen in figure A.2. Here is a list of the electrical connections corresponding to the various configurations adopted for the magnetic circuit, for the plasma grid bias and for polarisation of the bias plate.

- Configuration I: Old magnetic ciruit: the filter field is generated by current flowing through the Plasma grid and it returns to the power supply through the magnetic bias plate ($BP_m$). The PG can be biassed with respect to the body source, which is connected to the electric bias plate ($BP_e$).

- Configuration II: Old magnetic circuit, the filter field is generated in the same way as configuration I. The PG can be biassed with respect to the body source, but the $BP_e$ is floating.

- Configuration III: New magnetic circuit: the filter field is induced by current flowing through the PG and returning to the power supply through the C-shaped circuit, placed at 60 mm from the PG. The PG can be biassed as in former configurations. $BP_e$ and $BP_m$ are connected and floating.
- Configuration IV: New magnetic circuit: the filter field is induced by current flowing through the PG and returning to the power supply through both the C-shaped circuit and the $BP_m$. The Plasma Grid can be biassed as in former configurations. $BP_e$ is floating
- Configuration V: New magnetic circuit: the filter field is generated in the same way as configuration III. Plasma Grid can be biassed as in former configuration. Bias plate can be biased with respect to the PG by a power supply.

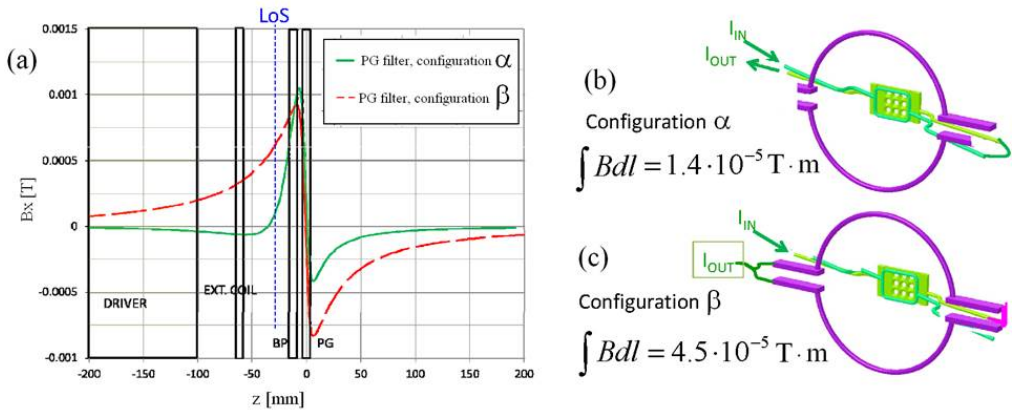


Figure A.1: a) Magnetic field generated by the magnetic circuits, b) the old magnetic circuit, c) the new magnetic circuit.

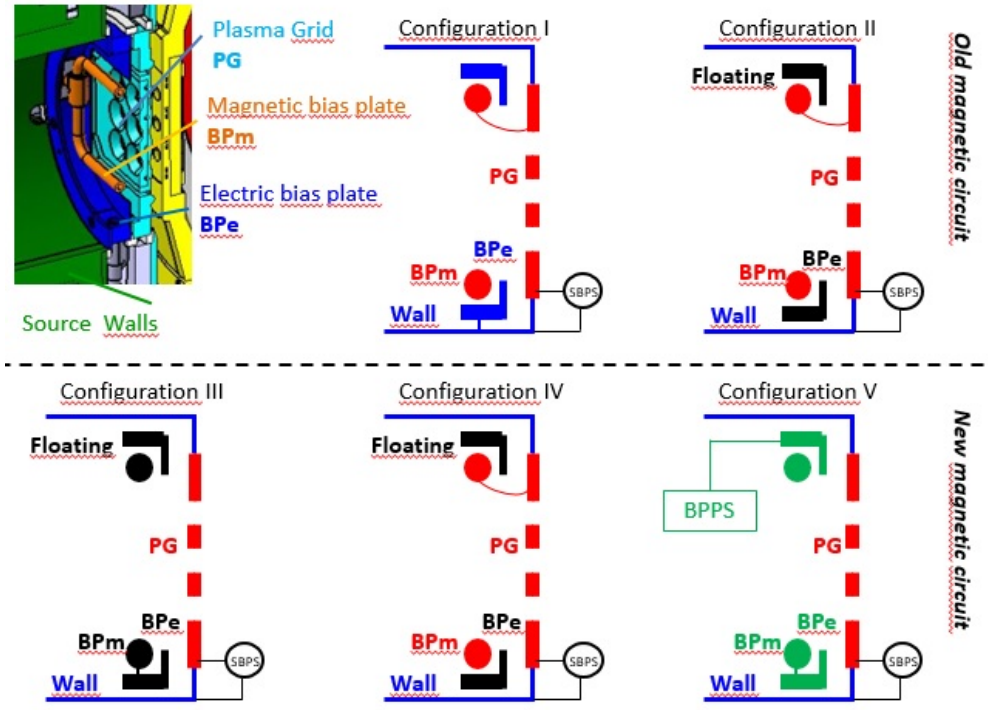


Figure A.2: Electric configurations

# Appendix B

# Reflected Power and density estimation

In sections 3.1 and 4.1 a brief analysis of reflected power in different pressure and input power conditions were exposed. Starting from this parameter, in this section a numerical method is proposed in order to evaluate the electronic density in the source. It is important to affirm that presently it is not possible to estimate the power ceded to the plasma. However, if future improvements will allow to obtain this parameter, the elctronic density can be estimated as proposed here.
From a circuital analyses, the reflected power can be used to obtain information about the electronic density in the driver zone. An attempt can be found in [24], using parameters which are presently not available in NIO1. An alternative way is here proposed, mainly based on numerical results exposed in [12], which involves parameters that will be measured in the future. Considering an inductively coupled plasma, its conductivity can be expressed as:

$$\sigma_P = \frac{e^2 n_e}{m_e} \frac{\nu_c - i\omega}{\nu_c^2 + \omega^2} \tag{B.1}$$

Plasma current and potential are

$$I_P = j\delta l = \sigma_P E_0 \delta l$$

$$V_P = 2\pi a E_0$$

From these equations, a relation between $I_P$ and $V_P$ can be obtained:

$$V_P = \frac{2\pi a}{\delta l} \frac{\nu_c + i\omega}{\epsilon_0 \omega_{pe}^2} I_P = (R_P + i\omega L_P) \tag{B.2}$$

$R_P$ and $L_P$ are respectively the plasma resistance and inductance and it is easy to

see that

$$R_P = \frac{2\pi a}{\delta l \sigma_{el}}$$
$$L_P = \frac{R_P}{\nu_c}$$

As written in [12], the total load impedence seen by the generator can be written as:

$$Z_L = R_L + i\omega L_L = \frac{V_{RF}}{I_{RF}} \tag{B.3}$$

This also can be written as:

$$Z_L = \left[R_{coil} + \frac{\omega^2 R_P L_{12}^2}{R_P^2 + \omega^2 (L_{22} + L_P)^2}\right] + i\omega \left[L_{11} - \frac{\omega^2 (L_{22} + L_P) L_{12}^2}{R_P^2 + \omega^2 (L_{22} + L_P)^2}\right] \tag{B.4}$$

Where $L_{11}$ is the self impedence of the coil, $L_{22}$ is the self impedence of the current sheet in the plasma, while $L_{12}$ is the mutual inductance. Those values are constant, as can be seen in Table (mettere tabella con valori).
Considering the absorbed power and the input power:

$$P_{abs} = \frac{1}{2} R_P I_P^2 \qquad P_{in} = \frac{1}{2} R_L I_{RF}^2 \tag{B.5}$$

Their ratio yields:

$$\frac{P_{abs}}{P_{in}} = \mathcal{R} = \frac{R_P}{R_L} \frac{\omega^2 L_{12}^2}{\omega^2 (L_{22} + L_P^2)^2 + R_P^2} \tag{B.6}$$

This relation can be simplified remembering the form of $R_L$, written in equation B.4 and it yields, after some calculations:

$$\mathcal{R} = \frac{R_P \omega^2 L_{12}^2}{R_P \omega^2 L_{12}^2 + R_{coil}(R_P^2 + \omega^2 (L_{22} + L_P)^2)} \tag{B.7}$$

Several factors depend on electronic density:

$$R_P = \frac{2\pi a}{\delta l \sigma_{el}} \qquad L_P = \frac{R_P}{\nu_c}$$

with

$$\sigma_{el} = \frac{e^2}{m_e \nu_c} n_e$$

A suitable numerical form for the skin depth can be found here [12]. It is:

$$\delta = \frac{\sqrt{2\epsilon_0 m_e}c}{e}\sqrt{\frac{1+\nu_c^2/\omega^2}{1+\sqrt{1+\nu_c^2/\omega^2}}}n_e^{-1/2}$$

$\nu_c$ itself depends on the electronic density: it has been estimated considering the work performed in [12]. Briefly, two terms contribute to the total collisional frequency: the first term is due to the collision between electrons and ions or neutral atoms. The second term is due to stochastic heating.

$$\nu_c = \nu_{ei} + \nu_{en} + \nu_{ion} + \nu_{stoc}$$

The first three terms have been widely treated in literature [23]; the last term has been fitted starting from functions in different stochastic regimes: [12].

$$\nu_{stoc} = 10^{-244.1+48.10log_{10}(x)-3.467log_{10}^2+0.1113log_{10}^3(x)-0.001336log_{10}^4(x)}$$

where $x = n_e T_e$.
If the electronic temperature is known, it is possible so solve numerically the system, thus obtaining the estimated electronic density.

# Bibliography


[1] ITER website *www.iter.org*

[2] M. Kikuchi, K. Lackner, Minh Quang Tran, *Fusion Physics*, International Atomic Energy Agency, Wien, 2012

[3] M. Bacal, G. W. Hamilton, *Phys. Rev. Lett.* **42** (1979) 1538

[4] J. Wessons, *Tokamaks, III Edition*, Oxford University Press, 2004

[5] G. Brown (Ed.): *The Physics and Technology of Ion Sources.* Weinheim: Wiley-VCH Verlag GmbH & Co. KGaA, 2004: pp. 159–187.

[6] M. Bacal and M Wada. *Negative hydrogen ion production mechanisms* , Applied physics reviews 2.2 (2015), p. 021305.

[7] P. Franzen et alii; *Progress of the development of the IPP RF negative ion source forthe ITER neutral beam system*, Nucl. Fusion **47** , 264 (2007)

[8] S. Humphries, Jr. : *Charged Particle Beams*, John Wiley and Sons.

[9] A. Theodore Forrester: *Large Ion Beams*, John Wiley and Sons.

[10] A. R. Choudhuri, *The physics of fluids and plasmas: an introduction for astrophysicists.* Cambridge University Press, 1998

[11] R. Hemsworth et al. "Status of the ITER heating neutral beam system". In: Nuclear Fusion 49.4 (2009), p. 045006

[12] M. Cazzador, *Analytical and numerical models and first operations on the negative ion source NIO1* Master Thesis, 2014, Università degli Studi di Padova

[13] M. A. Liebermann, *Principles of Plasma Discharges and Materials Processing*

[14] P. Sonato et alii, *The ITER full size plasma source device design*,Fusion Engineering and Design **84**, 2 (2009)

[15] M. Cavenago et alii; *Development of Versatile Multiaperture Negative Ion Sources*, AIP Conference Proceedings **1655**, 040006 (2015)

[16] M. Cavenago et alii; *First experiments with the negative ion source NIO1*, Review of Scientific Instruments **87** , 02B320 (2016)

[17] B. Zaniol et alii; *NIO1 Diagnostics*, AIP Conference Proceedings **1655**, 060010 (2015)

[18] M. Barbisan et alii; *Modeling and design of a beam emission spectroscopy diagnostic for the negative ion source NIO1*, Rev. Sci. Instrum. **85** 02A708 (2014)

[19] G. Serianni et alii; *Design, Installation, Commisioning and Operation of a Beamlet Monitor in the negative ion beam test stand at NIFS*, AIP Conference Proceedings **1655**, 060005 (2015)

[20] G. Serianni et alii; *Acquisition, Data Retrieval, Interlock and Control Systems for the Negative Ion Source NIO1*, Presented at NIBS 2016 Conference, Submitted to AIP Conf. Proc.

[21] http://www.farnell.com/datasheets/1669376.pdf

[22] A. Pimazzoni et alii; *A First Characterization of NIO1 Particle Beam by Means of a Diagnostic Calorimeter*, Presented at NIBS 2016 Conference, Submitted to AIP Conf. Proc.

[23] J. Yoon, M. Song, J. Han, S. Hwang, W. Chang, B. Lee, and Y. Itikawa: Cross Sections for Electron Collisions with Hydrogen Molecules. Journal of Physical and Chemical Reference Data, 37(2) (2008): p. 918. doi: 10.1063/1.2838023.

[24] M. Bandyopadhyay, Dass Sudhir and A. Chakraboborty, *Can we estimate plasma density in ICP driver through electrical parameters in RF circuit?*, AIP Conference Proceedings **1655**, 020013 (2015)

[25] NIST website, *www.nist.gov*

[26] M. Barbisan et alii; *Electron Density and Temperature in NIO1 RF Source, Operated in Oxygen and Argon*, Presented at NIBS 2016 Conference, Submitted to AIP Conf. Proc.

[27] H.P. Summers, *The ADAS User Manual*, v. 2.6 (2004), http://www.adas.ac.uk

[28] http://www.hamamatsu.com/eu/en/4016.html

[29] http://ridl.cfd.rit.edu/products/manuals/Acton/old/MANUAL/Sp-750i.pdf

[30] L. Tonks and I. Langmuir, *A General Theory of the Plasma of an Arc*, Phys. Rev. **34**, 876 (1929).

[31] M. Cavenago et alii; *Improvements of the Versatile Multiaperture Negative Ion Source NIO1*, Presented at NIBS 2016 Conference, Submitted to AIP Conf. Proc.

[32] N. Hershkowitz *How Langmuir Probes Work* , Plasma Diagnostics I, Academic Press,1989

[33] P. Veltri et alii, *Study of electron transport across the magnetic filter of NIO1 Negative ion Source* , Presented at NIBS 2016 Conference, Submitted to AIP Conf. Proc.